### nature physics

**Article** 

https://doi.org/10.1038/s41567-023-02221-1

# Biofilms as self-shaping growing nematics

Received: 7 October 2022

Accepted: 23 August 2023

Published online: 09 October 2023



Check for updates

Japinder Nijjer<sup>1,10</sup>, Changhao Li **©** <sup>2,10</sup>, Mrityunjay Kothari **©** <sup>3,4</sup>, Thomas Henzel<sup>3</sup>. Qiuting Zhang<sup>1</sup>, Jung-Shen B. Tai 10, Shuang Zhou 10, Tal Cohen 10, Shuang Zhou 10, Tal Cohen 10, T 

Active nematics are the non-equilibrium analogue of passive liquid crystals. They consist of anisotropic units that consume free energy to drive emergent behaviour. As with liquid crystal molecules in displays, ordering and dynamics in active nematics are sensitive to boundary conditions. However, unlike passive liquid crystals, active nematics have the potential to regulate their boundaries through self-generated stresses. Here we show how a three-dimensional, living nematic can actively shape itself and its boundary to regulate its internal architecture through growth-induced stresses, using bacterial biofilms confined by a hydrogel as a model system. We show that biofilms exhibit a sharp transition in shape from domes to lenses in response to changing environmental stiffness or cell-substrate friction, which is explained by a theoretical model that considers the competition between confinement and interfacial forces. The growth mode defines the progression of the boundary, which in turn determines the trajectories and spatial distribution of cell lineages. We further demonstrate that the evolving boundary and corresponding stress anisotropy define the orientational ordering of cells and the emergence of topological defects in the biofilm interior. Our findings may provide strategies for the development of programmed microbial consortia with emergent material properties.

Active nematics are collections of anisotropic particles that metabolize free energy to generate mechanical work. Unlike conventional liquid crystals (LCs), they exist far from equilibrium, and activity plays an important role in shaping their collective structure and dynamics<sup>1-6</sup>. One prototypical example of active nematics, with non-conserving particle number, is growing colonies of bacterial cells with elongated shapes<sup>7-13</sup>. When bacteria collectively secrete extracellular matrix to adhere to each other and a substrate, they form multicellular communities known as biofilms <sup>14,15</sup>. Biofilms grow in diverse environments including in the ocean, in soil and in humans, and as they develop, they take on a rich variety of three-dimensional (3D) morphologies, dynamics and internal architectures<sup>8,16-21</sup>. Moreover, the anisotropic shape of bacterial cells can lead to parallel alignment and non-trivial global organization, which allows one to use biofilms as model living nematic systems to probe the feedback between evolving boundaries and internal ordering<sup>22-24</sup>. Understanding this feedback could allow for controlled growth of beneficial biofilms, elimination of harmful ones and the potential development of a new class of growing active

<sup>1</sup>Department of Molecular, Cellular and Developmental Biology, Yale University, New Haven, CT, USA. <sup>2</sup>Department of Engineering Science and Mechanics, Pennsylvania State University, University Park, PA, USA. 3Department of Civil and Environmental Engineering, Massachusetts Institute of Technology, Cambridge, MA, USA. ⁴Department of Mechanical Engineering, University of New Hampshire, Durham, NH, USA. ⁵Department of Physics, University of Massachusetts Amherst, Amherst, MA, USA. Department of Mechanical Engineering, Massachusetts Institute of Technology, Cambridge, MA, USA. <sup>7</sup>Department of Biomedical Engineering, Pennsylvania State University, University Park, PA, USA. <sup>8</sup>Department of Materials Science and Engineering, Pennsylvania State University, University Park, PA, USA. 9Quantitative Biology Institute, Yale University, New Haven, CT, USA. 10These authors contributed equally: Japinder Nijjer, Changhao Li. Ze-mail: talco@mit.edu; suz10@psu.edu; jing.yan@yale.edu

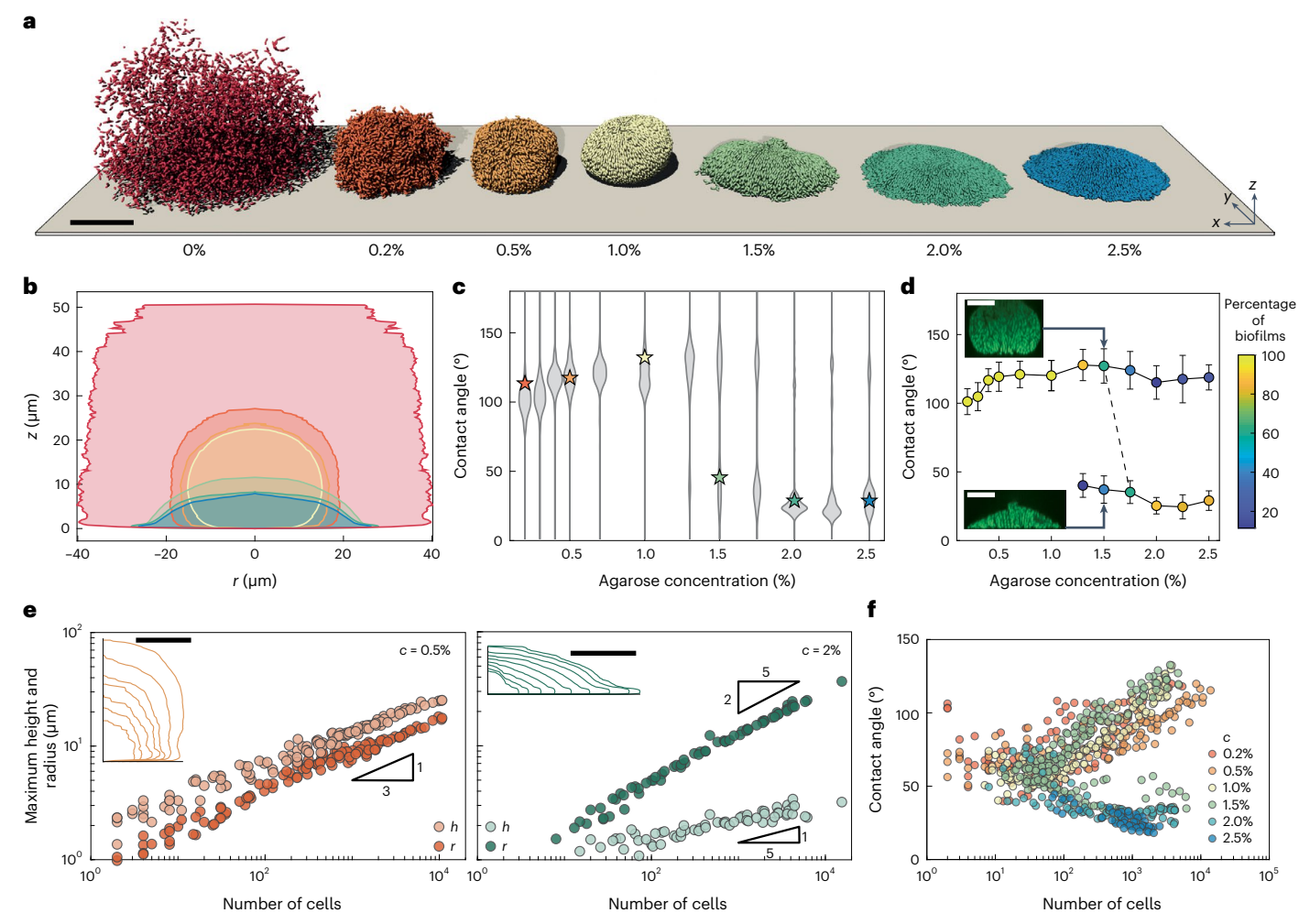


**Fig. 1**| **Biofilm shape bifurcation in response to environmental stiffness. a**, Reconstructed biofilms grown under agarose gels with different concentrations. Biofilms consist of  $8,600\pm700$  (mean  $\pm$  s.d.; range 7,245-9,420) cells. **b**, Shape of biofilms in **a** in cylindrical coordinates. The contours are reflected about r=0. **c**, Violin plot of contact angles calculated for biofilms grown under different agarose concentrations. Each chord represents a probability distribution function calculated from  $136\pm53$  (mean  $\pm$  s.d.; range 58-269) mature biofilms. Stars correspond to biofilms shown in **a** and **b**. **d**, Bifurcation of the biofilm contact angle with agarose concentration. Each point (and error

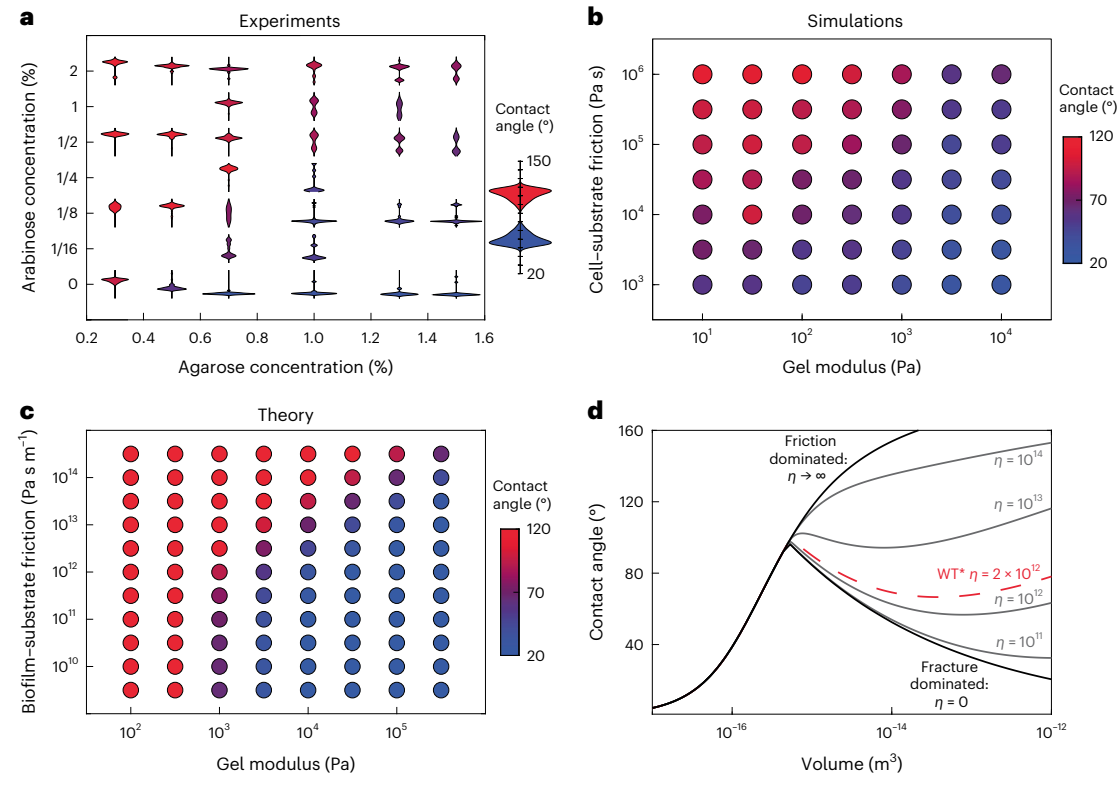
bar) corresponds to the mean (and standard deviation) of a gaussian fit that encompasses all biofilms with contact angles either greater than or less than 75° (underlying data are the same as for Fig. 1c). Insets: two examples of mature biofilms with different morphologies grown under 1.5% agarose gels. e, Plot of the maximum height and maximum radius of biofilms grown under a 0.5% gel (left) and 2% gel (right). Data correspond to ensembles of 12 and 6 different biofilms imaged over time, respectively. Inset: shape evolution of a single biofilm under each condition. f, Time-evolution of the contact angle for biofilms grown under gels with different stiffnesses. Scale bars, 10 μm.

materials that not only respond to but also actively alter their environment to maximize functionalities.

# Confinement and interfacial forces control morphogenesis

Here we use confined *Vibrio cholerae* biofilms as the model system to demonstrate the self-shaping and self-organizing capability of a 3D growing nematic system. To focus on the cell organization and biomechanical aspects of biofilm growth, we used a locked biofilm-forming strain, labelled WT\*16,25. To tune the effect of the boundary, we used a geometry in which the biofilm-forming bacteria were confined between a soft hydrogel and a stiff glass substrate<sup>16</sup>. We varied the stiffness of the overlaying gel by varying the agarose concentration (*c*) from 0.2% to 2.5%, resulting in shear moduli that ranged from 150 Pa to 150 kPa (Supplementary Fig. 1). In each case, the biofilms grew clonally from a single cell into a mature biofilm consisting of thousands of cells. Using time-lapse 3D imaging and cell-segmentation algorithms<sup>16,24</sup>, we extracted and tracked the evolution of biofilm

architectures at single-cell resolution (Extended Data Fig. 1 and Supplementary Videos 1-4). Figure 1a shows a series of segmented biofilms grown under gels of different concentrations, each consisting of roughly 8,600 cells. We found that as the biofilms matured, they developed into one of two bulk shapes, indicating two distinct growth modes: under soft confinement ( $c \le 1\%$ ), the biofilms grew as hemispherical structures, which we label 'domes', whereas under stiff confinement ( $c \ge 2\%$ ), the biofilms grew as flatter structures, which we label 'lenses' (Fig. 1b). At intermediate gel concentrations (1% < c < 2%), we observed the coexistence of both lenses and domes. To quantify this shape transition, we measured the contact angle  $(\psi)$  that the biofilms made with the glass substrate for hundreds of mature biofilms for each condition (Fig. 1c and Extended Data Figs. 2 and 3). Interestingly,  $\psi$  exhibited a bifurcation-like transition with increasing stiffness. Biofilms possessed larger  $\psi$  when grown under soft gels (median  $\psi$  range 101–121° for c = 0.2% to 1%) and smaller  $\psi$ when grown under stiff gels (median  $\psi$  range 23–39° for c = 2% to 2.5%); at intermediate concentrations (c = 1.3% to 1.75%), a bimodal



 $\label{lem:proposed} \textbf{Fig. 2} \ | \ \textbf{Environmental stiffness and biofilm-surface adhesion jointly control biofilm shape.} \ a, \ Phase diagram showing the experimental distribution of biofilm shapes for cells producing varying amounts of the surface adhesion protein Bap1, controlled by an arabinose-inducible promoter and grown in different stiffness environments. Each icon corresponds to a violin plot of contact angles, with red and blue corresponding to large and small mean contact angles, respectively. Each histogram corresponds to <math>41 \pm 25$  biofilms (mean  $\pm$  s.d.;

range 6–138). **b**, Phase diagram showing biofilm contact angles from ABSs for different cell–substrate friction coefficients and gel stiffnesses. Each dot corresponds to a single simulation. **c**, Phase diagram showing predicted biofilm contact angles calculated from the continuum model (Supplementary Note 2) for  $V = 10^{-13}$  m³. **d**, Predicted evolution of the contact angle with growing volume for stiffness  $\mu = 3$  kPa for different friction coefficients  $\eta$  (unit, Pa s m¹).

distribution of  $\psi$  emerged, with each peak coinciding with either the large  $\psi$  (small stiffness, median  $\psi$  range 127–131°) or small  $\psi$  (large stiffness, median  $\psi$  range 33–40°) behaviour (Fig. 1d).

In addition, the kinetics of shape evolution differed substantially between the two regimes, as quantified by the evolution of the maximum height  $h_{\rm max}$  and maximum radius  $r_{\rm max}$  of the biofilms (Fig. 1e). For soft confinement, the biofilms grew nearly isotropically, with the maximum height and radius scaling as  $h_{\rm max} \propto n^{1/3}$  and  $r_{\rm max} \propto n^{1/3}$ , respectively (where n is the number of cells). For stiff confinement, the biofilms grew faster horizontally than vertically, leading to an increasingly anisotropic shape over time. This was reflected in the different scaling laws for biofilm height and radius, where  $h_{\rm max} \propto n^{1/5}$  and  $r_{\rm max} \propto n^{2/5}$ , reminiscent of those observed during hydraulic fracturing  $^{26,27}$ . Correspondingly, we observed two diverging trajectories of  $\psi$  (Fig. 1f), where  $\psi$  either increased or decreased above -100 cells.

Previous work indicates cell–substrate friction as a key determinant in biofilm morphogenesis <sup>16,18,28,29</sup>, which in *V. cholerae* is primarily achieved by two redundant adhesion proteins RbmC and Bap1 (refs. 30–32). Upon deleting these adhesins, we found that the critical stiffness at which the shape transition occurred decreased (Extended Data Fig. 3). To further demonstrate the effect of cell–substrate friction on biofilm shape, we generated a strain with an arabinose-inducible expression vector with titratable expression of *bap1*. Indeed, as *bap1* expression increased, the critical stiffness at which the biofilms transitioned from domes to lenses also increased (Fig. 2a). A bimodal distribution of shapes was again observed near the phase boundary in the two-dimensional phase diagram. We also used experimentally benchmarked agent-based simulations (ABSs; Methods) to confirm

that the biofilm shape transition originated from the competition between surface friction and gel elasticity. Indeed, by varying only those two parameters, we reproduced the transition from large to small  $\psi$  upon decreasing friction or increasing gel stiffness (Fig. 2b and Supplementary Videos 5 and 6).

### An energetic model explains the biofilm shape transition

To elucidate the origins of the two different growth regimes, we consider the energetics of biofilm growth confined at the bonded interface between a semi-infinite elastic material and a rigid substrate, while accounting for the frictional losses the biofilm experiences as it slides along the substrate. Here we model the biofilm as a volumetrically expanding ideal liquid because on a long timescale, the biofilm can continuously reorganize its internal structure during growth 23,24,33,34. As the biofilm expands, it can deform the surrounding gel, delaminate the gel from the glass substrate or both. We consider the total potential energy of the system  $U = U_d + U_e$  as the sum of <sup>34</sup> (1) the adhesion energy  $U_{\rm d}(r_{\rm b}) = \Gamma \pi (r_{\rm b}^2 - r_{\rm i}^2)$  invested in delaminating the gel–glass interface with energy density Γ, starting from an initial basal radius of the biofilm  $r_i$  to its final basal radius  $r_b$ , and (2) the elastic energy stored in the gel  $U_e(r_b, V) = \mu r_b^3 f(V/r_b^3)$ , where  $\mu$  is the shear modulus and  $f = f(V/r_b^3)$  is the dimensionless elastic potential energy as a function of dimensionless volume, obtained from finite element simulations. Frictional forces come into play only after the gel begins to delaminate and the biofilm expands on the substrate, which we model using the Rayleigh dissipation function,  $D(r_b, \dot{r}_b) = \frac{1}{2} \int_0^{2\pi} \int_0^{r_b} \eta |\mathbf{v}(r; r_b, \dot{r}_b)|^2 r dr d\theta$ , where  $\eta$  is the friction coefficient and  $\mathbf{v}$  is the velocity of the biofilm at

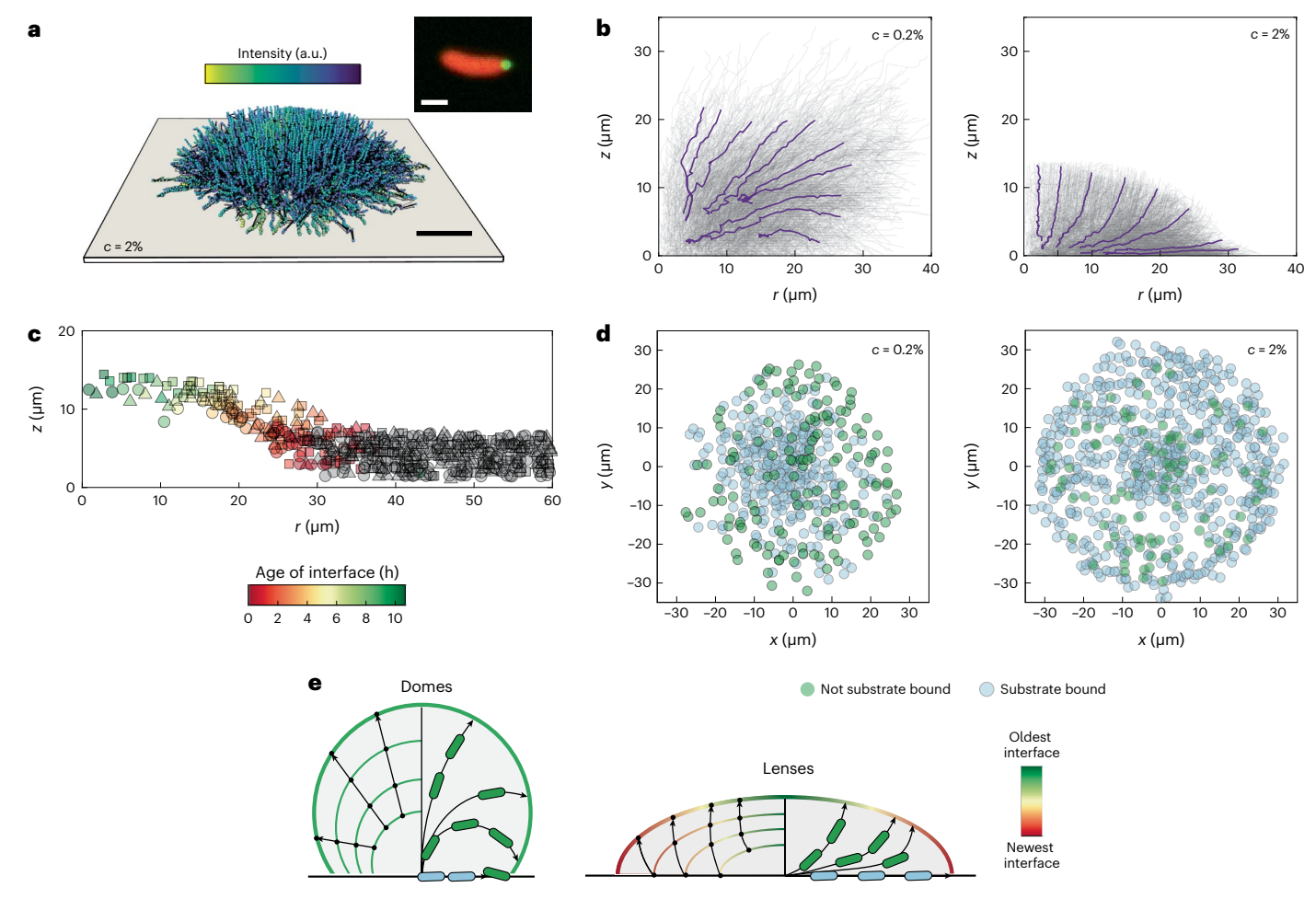


**Fig. 3** | **Boundary conditions dictate cell fate in biofilm. a**, Reconstructed cell trajectories from puncta tracking in a biofilm confined by a stiff gel (c = 2%). Colours denote the intensity of the fluorescently labelled puncta. Scale bar, 10 μm. Inset: image of a green-punctum-containing red V. *cholerae* cell. Scale bar, 1 μm. **b**, Puncta trajectories from biofilms grown under two different conditions projected into (r,z) space. Purple lines denote averaged trajectories that end near the edge of the biofilm. **c**, Age of the biofilm–gel interface measured by tracking the displacement of tracer particles embedded in the agarose gel.

The delamination time—that is, birth of the local interface—is defined as the time point when the vertical displacement of the corresponding tracer particle exceeds  $0.5\,\mu m$ . Data consist of an ensemble of three different biofilms labelled with three different markers.  $\boldsymbol{d}$ , Basal layer puncta labelled by whether their height has exceeded 3  $\mu m$  during their entire history, corresponding to cells that have transiently left the surface (green) and cells that are always substrate bound (blue), respectively.  $\boldsymbol{e}$ , Schematic representation of the cell trajectories and their coupling to boundary evolution.

the substrate. The Euler–Lagrange equation for this system, with the generalized coordinate  $r_b \equiv r_b(V)$ , is written as  $\frac{\partial U}{\partial r_b} = -\frac{\partial D}{\partial r_b}$ , which gives

$$H\frac{\mathrm{d}\tilde{r}_{b}}{\mathrm{d}\widetilde{V}} = M\frac{\widetilde{F}\left(\widetilde{V}/\widetilde{r}_{b}^{3}\right)}{\widetilde{V}} - \frac{1}{\widetilde{V}\tilde{r}_{b}} \tag{1}$$

where  $\tilde{r}_b \equiv r_b/r_i$  and  $\widetilde{V} \equiv V/r_i^3$  are dimensionless quantities and  $\tilde{F}(x) = xf'(x) - f(x)$  (Supplementary Note 2). Crucially, the biofilm growth dynamics are governed by two dimensionless variables that emerge naturally from this formulation: the dimensionless friction  $H = \eta g r_i^2/4\Gamma$  (where g is the biofilm growth rate) and the dimensionless elastic modulus  $M = 3\mu r_i/2\pi\Gamma$ , which measure the relative importance of frictional dissipation and elastic potential energy to interfacial energy, respectively. Solving equation (1), we find that as the volume increases, the system initially exhibits cavitation-like expansion during which biofilm growth induces only elastic deformation in the gel with no sliding motion of the biofilm with respect to the substrate, along with a growing contact angle  $^{34}$ . The system then transitions to delamination during which breakage of interfacial bonds between the gel

and the glass substrate becomes energetically favourable and leads to sliding of the biofilm cells along the substrate. In this limit, biofilm growth mimics a 'hydraulic fracture' 26,27, which gives rise to a decreasing contact angle and a lens-shaped biofilm. Finally, as the biofilm continues to grow, the system transitions to a friction-limited delamination regime in which friction retards expansion on the substrate leading to a growing contact angle again and hence a dome-shaped biofilm (Fig. 2d). Experimentally, the observed contact angles of biofilms are controlled by V,  $\eta$  and  $\mu$ . Benchmarked by experimentally measured values (Supplementary Note 2), the theoretical phase diagram closely matches those attained experimentally and recapitulates many salient features (Fig. 2c, Extended Data Fig. 4 and Supplementary Fig. 2). In the small  $\eta$  limit, the model reduces to the previous interfacial cavitation model<sup>34</sup> in which the shape is independent of  $\eta$ . In the large  $\eta$  limit, this model predicts that the shape transition occurs at a constant ratio of  $\eta$  to  $\mu$ , consistent with the ABS results quantitatively and with the bap1-titration experiment qualitatively; in this limit, the energetics is dominated by the balance between the frictional dissipation and elastic deformation of the gel, so the shape only depends on  $H/M = (\pi g r_i/6)(\eta/\mu)$ .

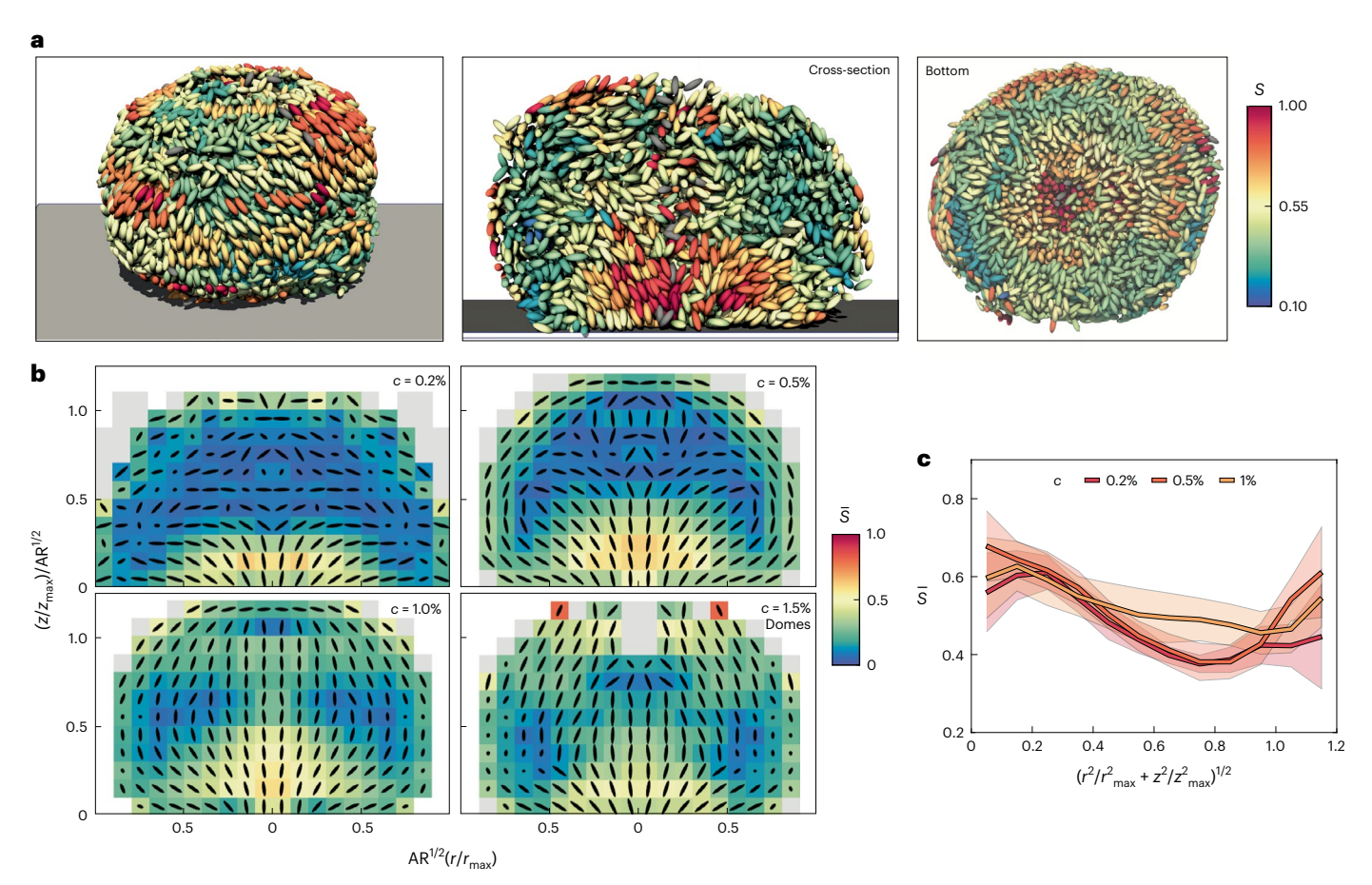


**Fig. 4** | **3D** spatial variation in cell orientations and ordering in dome-shaped biofilms. **a**, Three-dimensional reconstruction of a biofilm grown under soft confinement (c = 0.5%). Cells are coloured on the basis of the scalar order parameter calculated in each differential volume with  $\Delta r = 2 \, \mu m$ ,  $\Delta z = 2 \, \mu m$ , and angular extent  $\Delta \theta = 45^\circ$ . **b**, Azimuthally averaged cell orientations for biofilms grown in different stiffness environments. Colours denote the scalar order parameter, and the ovals denote the average direction of the cells projected into (r,z) space. Data are first averaged azimuthally in each biofilm and then averaged across  $13 \pm 5$  (mean  $\pm$  s.d.; range 5–18) different biofilms. To account for different

sizes of biofilms, r and z were rescaled by  $r_{\rm max}$  and  $z_{\rm max}$  prior to averaging and rescaled after averaging such that the aspect ratio was equal to the mean aspect ratios (AR) of the underlying biofilms. Note that the data shown are reflected about r=0. Grey denotes regions with an insufficient number of cells for averaging.  ${\bf c}$ , Scalar order parameter averaged as a function of the normalized distance to the origin (mean  $\pm$  s.d.). For each condition, data are first averaged in each biofilm and then averaged across biofilms (data correspond to the same underlying data as in  ${\bf b}$ ).

#### Boundary evolution determines cell trajectories

As a biofilm grows, the dwelling cells can self-organize spatially and temporally; we therefore considered the implications of the different morphologies on the internal structural evolution of the biofilm. Critical to understanding this self-organization process is revealing the trajectories of different cells inside the biofilm. To this end, we used a bacterial strain in which each cell contained a single bright punctum<sup>35,36</sup> that we tracked over time (Fig. 3a and Supplementary Video 7). We projected all trajectories into the axisymmetric coordinates of the biofilm (Fig. 3b, grey lines) and overlaid them with the averaged trajectories for cells that ended near the boundary (Fig. 3b, purple lines). This allowed us to visualize the spatial distribution of different cell lineages.

Under soft confinement, cell trajectories followed a fountain-like flow pattern in which cells that originated near the core left the substrate and overtook frictionally slowed cells near the substrate (Fig. 3b,d), in a manner similar to unconfined biofilms<sup>36</sup>. In contrast, when the gel was stiff, all cell trajectories bent upwards, away from the substrate (Fig. 3b); as a direct consequence, the basal layer of the biofilm consisted primarily of cell lineages that always stayed on the substrate (Fig. 3d). A similar change in cell trajectories was observed in the ABSs upon changing biofilm morphology, therefore ruling out

biological signalling as the cause of the observed change in cell trajectories (Extended Data Fig. 5).

We hypothesized that the observed alteration in cell trajectories was driven by the differing progressions of the biofilm-gel boundary. This is because the cells at the boundary are anchored to the  $gel^{24}$ , requiring the cells to track the motion of that material point. To support this hypothesis, we tracked the displacements of the boundary by embedding and tracking tracer particles in the agarose gel (Supplementary Video 8). Consistent with our theoretical model for the overall shape, we found two distinct modes of tracer trajectories corresponding to the dome-shaped and lens-shaped modes of growth (Extended Data Fig. 6). In the stiff gel (lens-shaped) regime, the tracers were displaced vertically away from the substrate as the gel delaminated to continuously create new biofilm-gel and biofilm-glass interfaces; in contrast, in the soft gel (dome-shaped) regime, little new biofilmglass interface was created, and instead the biofilm-gel boundary expanded to accommodate cell proliferation. To reveal the creation of new interface in the stiff gel regime, we mapped the 'age' of the biofilm-gel interface (Fig. 3c) and found that the central part of the interface was indeed older because it was created earlier during biofilm growth. Because a cell adhered to the gel boundary will track the boundary displacement, this naturally leads to upward bending of the

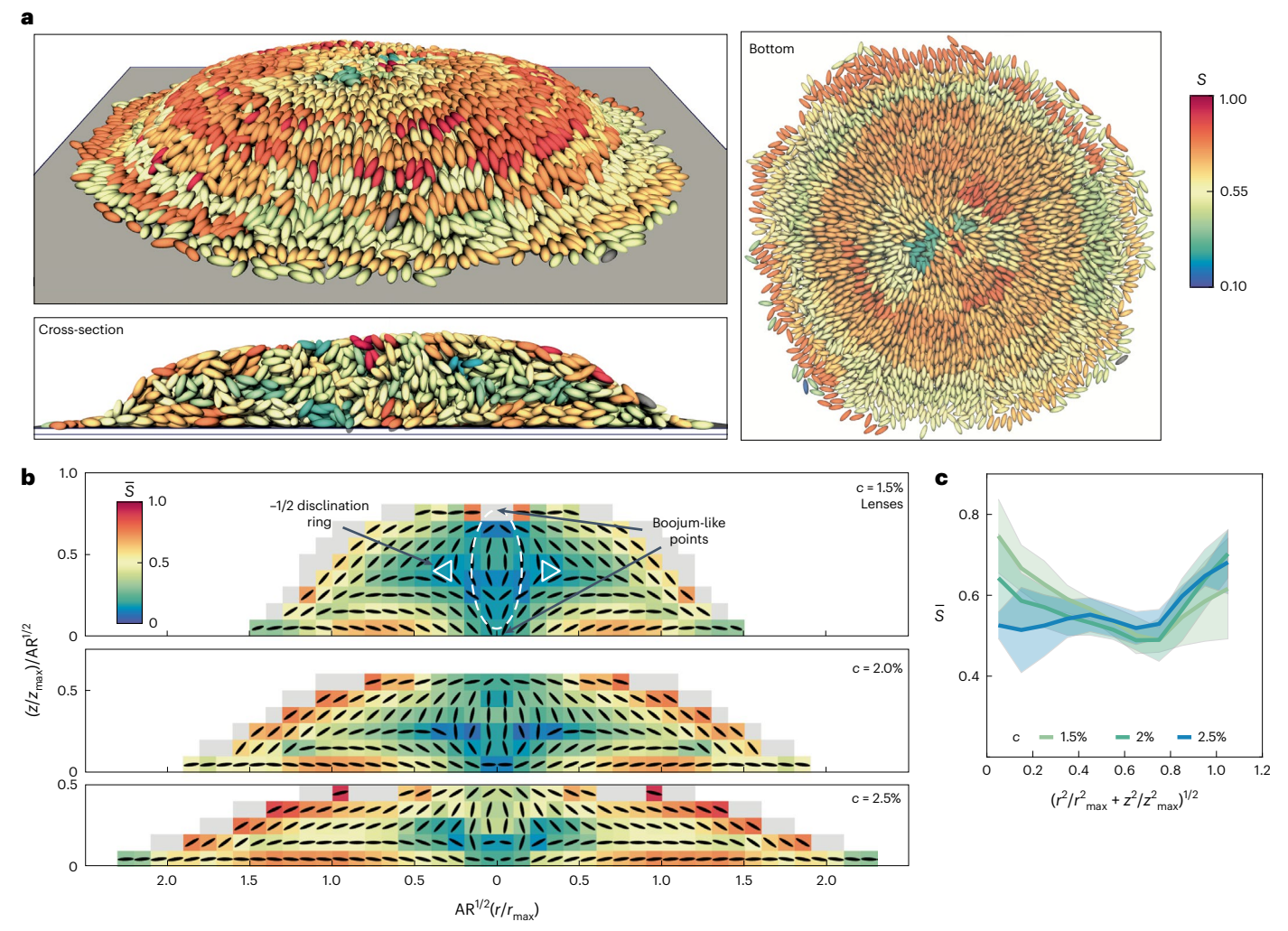


**Fig. 5** | **3D** spatial variation in cell orientations and ordering in lens-shaped biofilms. **a**, Three-dimensional reconstruction of a biofilm grown under stiff confinement (c = 2%). Cells are coloured on the basis of the scalar order parameter calculated in each differential volume, with  $\Delta r = 2 \, \mu m$ ,  $\Delta z = 2 \, \mu m$ ,  $\Delta \theta = 45^\circ$ . **b**, Azimuthally averaged cell orientations for biofilms grown in different stiffness environments. Colours denote the scalar order parameter, and

ovals denote the average direction of the cells projected into (r,z) space. Data are first averaged azimuthally in each biofilm and then averaged across  $11\pm 4$  (mean  $\pm$  s.d.; range 6–16) different biofilms. Grey denotes regions with an insufficient number of cells for averaging.  ${\bf c}$ , Scalar order parameter averaged as a function of the normalized distance to the origin (mean  $\pm$  s.d.).

cell trajectories in the lens-shaped limit (Fig. 3e). Lending support to this argument, when we deleted the key exopolysaccharide biogenesis gene *vpsL* such that cells were not adhesive to the boundaries<sup>24,37</sup>, the cell trajectories no longer bent upwards despite the fact that the biofilm was similarly lens-shaped (Extended Data Fig. 7). Therefore, we conclude that progression of the biofilm–gel boundary combined with cell–gel adhesion determines the positional cell fate and the spatiotemporal distribution of lineages in a biofilm.

## Stress anisotropy controls nematic structural transition

A hallmark of LCs is the self-organization of orientational order due to anisotropic interparticle interactions. The ground state of an unconfined nematic assumes a constant scalar order parameter  $S(\mathbf{r})$  and a uniform director  $\hat{\mathbf{n}}(\mathbf{r})$  (ref. 38); when a nematic is confined, however, the anchoring condition at the boundary can often lead to geometric frustrations and creation of topological defects 39,40. Given the elongated shape of V. cholerae cells, a natural question is how the evolving biofilm boundary influences the orientational order inside the biofilm. To quantify the orientational order, we measured the spatially varying

nematic order parameter tensor  $Q(\mathbf{r}) = \langle 3\hat{\mathbf{n}}_i \otimes \hat{\mathbf{n}}_i - I \rangle /2$ , where angled brackets denote spatial averaging across cell orientations  $\hat{\mathbf{n}}_i$  of different cells i in a local neighbourhood (Figs. 4 and 5) and I is the identity matrix. The scalar order parameter S was defined as the maximum eigenvalue of Q, and the non-polar director  $\hat{\mathbf{n}}(\mathbf{r}) = -\hat{\mathbf{n}}(\mathbf{r})$ , which marked the averaged local orientation of cells, was the corresponding eigenvector. Under this definition, when S=1, cells are aligned perfectly parallel to each other, and when S=0, the cell orientations are isotropically disordered.

We measured  $Q(\mathbf{r})$  in 6–18 biofilms at each gel concentration and averaged them to generate 'prototypes' of biofilm organization and obtained the locally averaged nematic order parameters  $\bar{S}(r,z)$  and  $\bar{\mathbf{n}}(r,z)$  (Figs. 4 and 5 and Extended Data Fig. 8). As the gel concentration increased from 0.2% to 1.5%,  $\bar{S}$  of the dome-shaped biofilm increased. In general,  $\bar{S}$  was maximized at the origin, where  $\bar{S}\approx 0.6$ , and gradually reduced to as low as 0.4 but increased again to -0.6 at the gel boundary (Fig. 4c). For the higher gel concentrations (c=1.0% and 1.5%), the director field followed a 'bipolar' structure with two surface defects, called boojums, sitting at the origin and apex of the biofilm, similar to those observed in thermotropic LCs confined in a spherical droplet

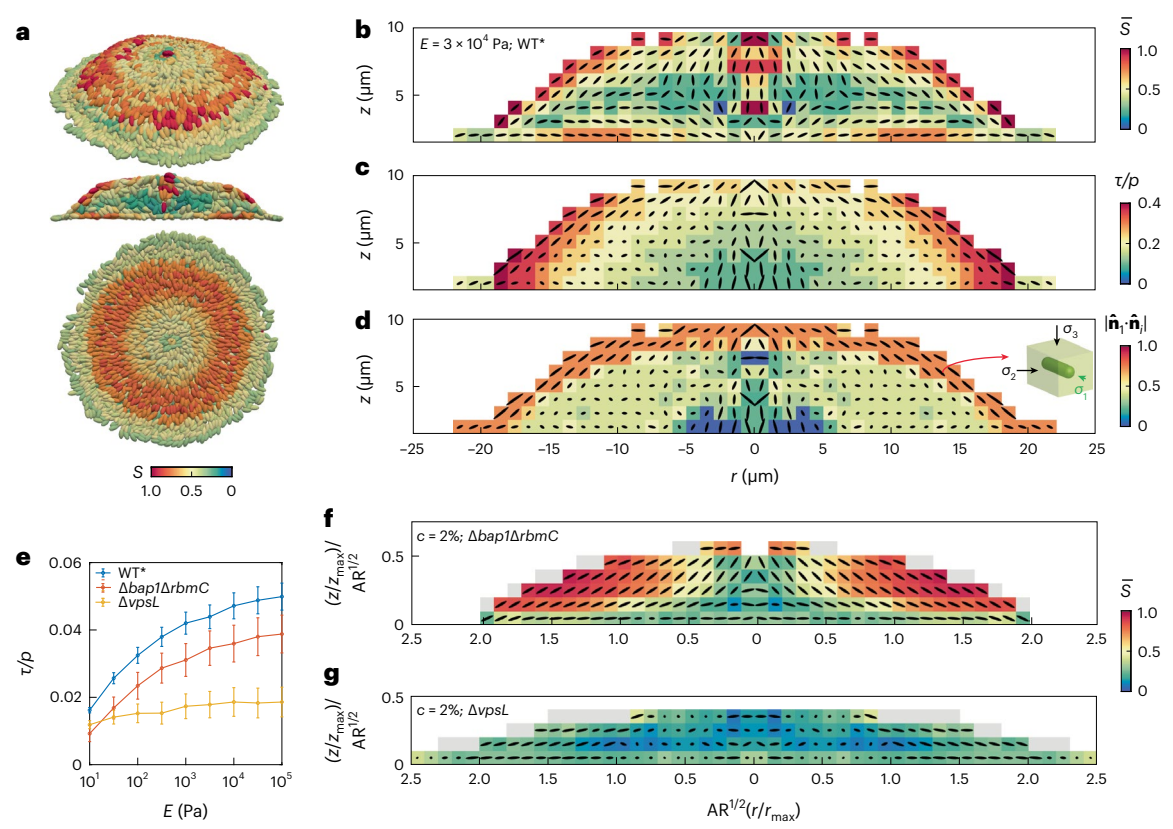


Fig. 6 | ABSs recapitulate the experimental cellular ordering and reveal stress anisotropy in biofilms. a, Oblique, cross-sectional and bottom views of a representative simulated biofilm grown under stiff confinement (gel modulus  $E\approx 10^4$  Pa). Cells are coloured on the basis of the scalar order parameter calculated in each differential volume, with  $\Delta r=2~\mu$ m,  $\Delta z=2~\mu$ m,  $\Delta \theta=45^\circ$ . b, Azimuthally averaged cell orientations for the same simulated biofilm as in a. Colours denote the scalar order parameter, and ovals denote the average director of the cells projected into (r,z) space. c, Azimuthally averaged first principal stress direction  $\hat{\bf n}_1$ , where colours denote the stress anisotropic parameter  $\tau/p$ . Ovals denote the unit orientation vector corresponding to  $\sigma_1$  projected into (r,z)

space. **d**, Azimuthally averaged alignment between the cell direction and first principal stress direction,  $|\hat{\mathbf{n}}_1 \cdot \hat{\mathbf{n}}_i|$ . Ovals denote the unit orientation vector corresponding to  $\sigma_1$  projected into (r,z) space. **e**, Stress anisotropy  $\tau/p$  as a function of the gel modulus E for simulations with both cell–substrate friction and cell–gel adhesion, with cell–gel adhesion only and with neither cell–substrate friction nor cell–gel adhesion, corresponding to WT\*,  $\Delta bap1\Delta rbmC$  and  $\Delta vpsL$  biofilms, respectively. Each data point corresponds to the mean  $\pm$  s.d. of eight unique simulations. **f**.g, Azimuthally averaged cell orientations for  $\Delta bap1\Delta rbmC$  (**f**) and  $\Delta vpsL$  (**g**) mutant biofilms (experiment) grown under 2% agarose gel, with a total of six and seven biofilms averaged, respectively.

with planar anchoring (Fig. 5) $^{40,41}$ . Concomitant with the dome-to-lens shape transition at c=1.5%, we observed a marked topological transition of the director field. In lens-shaped biofilms, the two boojums remained and the director connecting the two boojums bent smoothly in the middle of the biofilm (Fig. 5b); however, an additional –1/2 disclination loop emerged around this ellipsoid, making them topologically distinct from the dome-shaped biofilms.  $\bar{S}$  was generally higher in lens-shaped biofilms but still showed a small dip in the interior (Fig. 5c).

Previously, using a combination of ABS and continuum modelling, it was shown that biofilm growth on a rigid substrate leads to large compressive stresses driving a core of verticalized cells<sup>31,42</sup>, while the surrounding growth-induced flow leads to horizontal, radially aligned cells<sup>16</sup>. Although these results define the ordering on the basal boundary, they do not explain the cell organization in the bulk. Using experimentally benchmarked parameters, we were able to recapitulate the cell ordering in the entire biofilm using ABSs (Fig. 6a,b), which enabled us to interrogate the mechanical stress  $\sigma$  experienced by each individual bacterium. Crucially, we found the existence of substantial stress anisotropy in confined biofilms, quantified as  $\tau/p$ , where  $p = \operatorname{tr}(\sigma)/3$ and  $\tau = \sqrt{2/3(\sigma - pI) : (\sigma - pI)}$ . This anisotropy was strongest at the biofilm-gel interface and propagated gradually into the interior (Fig. 6c). Since elastic strain energy for a rod-shaped cell arises predominantly from compression along its long axis, the cell's most energetically stable state is when the cell orientation,  $\hat{\mathbf{n}}_i$ , aligns with the direction of minimal compressive stress. Defining the three principal stresses,  $0 \ge \sigma_1 \ge \sigma_2 \ge \sigma_3$  (Fig. 6d, inset), cells will therefore align with the direction of the first principal stress,  $\hat{\bf n}_1$ . This argument is a generalized statement of stress anisotropy-induced alignment previously proposed to explain cell ordering in two-dimensional bacterial colonies<sup>43</sup>. Defining the relative orientation parameter  $\alpha_i = |\hat{\bf n}_{1,i}\cdot\hat{\bf n}_i|$  as the degree of alignment between cell orientation and the first principal stress, we found that, indeed, regions of high  $\alpha$  largely coincided with regions of high stress anisotropy (Fig. 6d). The reason for the strong alignment at the biofilm–gel interface is that as the biofilm grows and the biofilm–gel interfacial area dilates, a shear force resisting the relative motion between the cells and gel develops at this interface<sup>24</sup>. The corresponding shear stress acting on the cells leads to large stress anisotropy, where  $\hat{\bf n}_1$  points towards the polar direction, therefore aligning the cells bipolarly near the biofilm–gel interface (Fig. 6b,c).

Interestingly, cells at the biofilm–glass interface do not align with the first principal stress (Fig. 6c). This is likely due to the high hydrostatic pressure *p* in the biofilm centre (Extended Data Fig. 9), which leads to closer packing of the soft rods (Supplementary Fig. 2) and hinders cell rotations<sup>44</sup>. More importantly, because the glass substrate does not deform and remains flat, it cannot generate more shear force to the glass-adhered cells due to areal dilation; therefore, the interfacial stress-induced alignment mechanism is absent at this interface. Instead, a flow-induced alignment model was previously

used to accurately capture the radial alignment at the biofilm–glass interface<sup>16</sup>. The ordering at the two interfaces (biofilm–gel and biofilm–glass), controlled by two different mechanisms, defines the biofilm's internal architecture together with the shape of the biofilm.

We further propose that the key difference in cell ordering between lens- and dome-shaped biofilms can be explained by the different ordering at the triple-contact point where the two boundaries meet, which is in turn controlled by the bulk energetics (see above). For  $\psi > 90^\circ$  (dome-shaped biofilms, Fig. 4b),  $\hat{\bf n}$  smoothly transitions from the biofilm–glass to the biofilm–gel interface such that no topological defects are necessary in the interior; only two boojums are found at the top and bottom of the biofilm surface. In contrast, for  $\psi < 50^\circ$  (lens-shaped biofilms, Fig. 5b), a splay conformation is required at the triple-contact point to smoothly transition from one interface to the other. This necessitates a defect of charge -1 in the interior of the biofilm since a splay at the triple-contact point leads to a total angular change of  $-2\pi$  as one traverses the boundary clockwise. This topological constraint is satisfied by a defect ring of charge -1/2.

To validate this proposed mechanism, we first confirm with ABSs that cells far from the interfaces experience nearly vanishing shear stress but high hydrostatic compression (Fig. 6b,c), leading to low  $\bar{S}(r)$ in the middle of the biofilm. Second, the averaged shear stress and the associated anisotropy increase as gel stiffness increases (Fig. 6e), leading to overall higher  $\bar{S}$  in both the simulation and experiments. Third, when we removed the radial ordering at the biofilm-glass interface by deleting the cell-substrate adhesion16, the -1/2 disclination loop disappeared and the boundary-driven alignment from the top penetrated deeper into the biofilm (Fig. 6f and Extended Data Fig. 9). Finally, by deleting the biofilm extracellular matrix (ΔυpsL mutant) and therefore removing both cell-substrate and cell-gel adhesion<sup>16,37</sup>, the shear stress anisotropy decreases throughout the biofilm, the first principal stress points in random directions, and, consequently, cells are randomly oriented (Fig. 6g and Extended Data Fig. 9), similar to classical bacterial  $colonies \hbox{$^{7,9,12,13,45}$.} \ To sum up, our results demonstrate how biofilm shape$ and cellular configuration at the boundary, set by the joint effects of macroscopic energetics and microscopic stress anisotropy, drive the emergence of distinct long-range nematic ordering in the interior of biofilms.

#### Conclusion

Understanding the different modes of biofilm growth is critical to understanding how biofilms and, more generally, growing organisms can alter their morphology and internal architecture in response to environmental signals and constraints. This is also useful when engineering new classes of growing active materials that adapt to their surroundings by considering the interplay between bulk shape and internal organization. Here we showed how a growing biofilm actively shapes its environment and its internal architecture and lineages through mechanical coupling to its surroundings. The physical processes of self-shaping and self-organization in biofilm have several biological implications. For example, a mature lens-shaped biofilm can take advantage of the delamination process to create empty space beyond the edge of the biofilm, allowing cells to disperse 46 and explore new territory (Extended Data Fig. 10a,b). When a number of biofilms grew in proximity to each other, the cumulative stresses generated by many biofilms led to large-scale, collective delamination of the gel from the substrate, leading to a 'village' of biofilm clusters interspersed with free-swimming cells (Extended Data Fig. 10c-e). Moreover, because the geometry and directionality of cell growth dictate the accessibility of nutrients to the entire biofilm, nematic cell ordering may afford improved nutrient/ waste diffusion into and out of the innermost portions of the biofilm<sup>47</sup>. Different cell trajectory patterns will transport different lineages to separate regions of the biofilm and determine where antibiotic tolerant or persistent cells end up spatially in the biofilm<sup>48</sup>. The variation in cell positional fate could further couple with heterogeneous gene

expression patterns in the biofilm, leading to segregation of cells with different internal states  $^{11,36,49}$ . From an application point of view, the phenomena discovered here could offer new ways to mechanically guide biofilm growth, leading to new strategies to suppress the growth of harmful biofilms and to design and program beneficial ones. Finally, while in this work we manipulated extracellular matrix production through mutagenesis, it is intriguing to consider how and when bacteria adapt extracellular matrix production to mechanical cues through gene regulation to guide their own development  $^{15}$ .

#### **Online content**

Any methods, additional references, Nature Portfolio reporting summaries, source data, extended data, supplementary information, acknowledgements, peer review information; details of author contributions and competing interests; and statements of data and code availability are available at https://doi.org/10.1038/s41567-023-02221-1.

#### References

- Sanchez, T., Chen, D. T. N., DeCamp, S. J., Heymann, M. & Dogic, Z. Spontaneous motion in hierarchically assembled active matter. Nature 491, 431–434 (2012).
- Needleman, D. & Dogic, Z. Active matter at the interface between materials science and cell biology. Nat. Rev. Mater. 2, 17048 (2017).
- Doostmohammadi, A., Ignés-Mullol, J., Yeomans, J. M. & Sagués, F. Active nematics. Nat. Commun. 9, 3246 (2018).
- Duclos, G. et al. Topological structure and dynamics of threedimensional active nematics. Science 367, 1120–1124 (2020).
- Copenhagen, K., Alert, R., Wingreen, N. S. & Shaevitz, J. W. Topological defects promote layer formation in Myxococcus xanthus colonies. Nat. Phys. 17, 211–215 (2021).
- 6. Saw, T. B. et al. Topological defects in epithelia govern cell death and extrusion. *Nature* **544**, 212–216 (2017).
- Dell'Arciprete, D. et al. A growing bacterial colony in two dimensions as an active nematic. Nat. Commun. 9, 4190 (2018).
- Yaman, Y. I., Demir, E., Vetter, R. & Kocabas, A. Emergence of active nematics in chaining bacterial biofilms. *Nat. Commun.* 10, 2285 (2019).
- Su, P.-T. et al. Bacterial colony from two-dimensional division to three-dimensional development. PLoS ONE 7, e48098 (2012).
- Volfson, D., Cookson, S., Hasty, J. & Tsimring, L. S. Biomechanical ordering of dense cell populations. *Proc. Natl Acad. Sci. USA* 105, 15346–15351 (2008).
- Dhar, J., Thai, A. L. P., Ghoshal, A., Giomi, L. & Sengupta, A. Self-regulation of phenotypic noise synchronizes emergent organization and active transport in confluent microbial environments. *Nat. Phys.* 18, 945–951 (2022).
- Doostmohammadi, A., Thampi, S. P. & Yeomans, J. M. Defect-mediated morphologies in growing cell colonies. *Phys. Rev. Lett.* 117, 048102 (2016).
- Warren, M. R. et al. Spatiotemporal establishment of dense bacterial colonies growing on hard agar. eLife 8, e41093 (2019).
- Hall-Stoodley, L., Costerton, J. W. & Stoodley, P. Bacterial biofilms: from the natural environment to infectious diseases. *Nat. Rev. Microbiol.* 2, 95–108 (2004).
- 15. Flemming, H.-C. et al. Biofilms: an emergent form of bacterial life. *Nat. Rev. Microbiol.* **14**, 563–575 (2016).
- Nijjer, J. et al. Mechanical forces drive a reorientation cascade leading to biofilm self-patterning. Nat. Commun. 12, 6632 (2021).
- Hartmann, R. et al. Emergence of three-dimensional order and structure in growing biofilms. Nat. Phys. 15, 251–256 (2019).
- Yan, J., Sharo, A. G., Stone, H. A., Wingreen, N. S. & Bassler, B. L. Vibrio cholerae biofilm growth program and architecture revealed by single-cell live imaging. Proc. Natl Acad. Sci. USA 113, e5337–e5343 (2016).

- Drescher, K. et al. Architectural transitions in Vibrio cholerae biofilms at single-cell resolution. Proc. Natl Acad. Sci. USA 113, e2066–e2072 (2016).
- Xu, H., Huang, Y., Zhang, R. & Wu, Y. Autonomous waves and global motion modes in living active solids. *Nat. Phys.* 16, 46–51 (2022).
- 21. Pearce, P. et al. Flow-induced symmetry breaking in growing bacterial biofilms. *Phys. Rev. Lett.* **123**, 258101 (2019).
- Dufrêne, Y. F. & Persat, A. Mechanomicrobiology: how bacteria sense and respond to forces. *Nat. Rev. Microbiol.* 18, 227–240 (2020).
- Fortune, G. T., Oliveira, N. M. & Goldstein, R. E. Biofilm growth under elastic confinement. *Phys. Rev. Lett.* 128, 178102 (2022).
- Zhang, Q. et al. Morphogenesis and cell ordering in confined bacterial biofilms. Proc. Natl Acad. Sci. USA 118, e2107107118 (2021).
- Beyhan, S. & Yildiz, F. H. Smooth to rugose phase variation in Vibrio cholerae can be mediated by a single nucleotide change that targets c-di-GMP signalling pathway. Mol. Microbiol. 63, 995–1007 (2007).
- O'Keeffe, N. J., Huppert, H. E. & Linden, P. F. Experimental exploration of fluid-driven cracks in brittle hydrogels. *J. Fluid Mech.* 844, 435–458 (2018).
- 27. Lai, C.-Y., Zheng, Z., Dressaire, E. & Stone, H. A. Fluid-driven cracks in an elastic matrix in the toughness-dominated limit. *Phil. Trans. R. Soc. A* **374**, 20150425 (2016).
- Fei, C. et al. Nonuniform growth and surface friction determine bacterial biofilm morphology on soft substrates. *Proc. Natl Acad.* Sci. USA 117, 7622–7632 (2020).
- Beroz, F. et al. Verticalization of bacterial biofilms. Nat. Phys. 14, 954–960 (2018).
- Teschler, J. K. et al. Living in the matrix: assembly and control of Vibrio cholerae biofilms. Nat. Rev. Microbiol. 13, 255–268 (2015).
- 31. Berk, V. et al. Molecular architecture and assembly principles of *Vibrio cholerae* biofilms. *Science* **337**, 236–239 (2012).
- Huang, X. et al. Vibrio cholerae biofilms use modular adhesins with glycan-targeting and nonspecific surface binding domains for colonization. Nat. Commun. 14, 2104 (2023).
- Li, J. et al. Nonlinear inclusion theory with application to the growth and morphogenesis of a confined body. J. Mech. Phys. Solids 159, 104709 (2022).
- Henzel, T. et al. Interfacial cavitation. PNAS Nexus 1, pgac217 (2022).
- 35. Parry, B. R. et al. The bacterial cytoplasm has glass-like properties and is fluidized by metabolic activity. *Cell* **156**, 183–194 (2014).
- Qin, B. et al. Cell position fates and collective fountain flow in bacterial biofilms revealed by light-sheet microscopy. Science 369, 71–77 (2020).

- Fong, J. C. N., Syed, K. A., Klose, K. E. & Yildiz, F. H. Role of Vibrio polysaccharide (vps) genes in VPS production, biofilm formation and Vibrio cholerae pathogenesis. Microbiology 156, 2757–2769 (2010).
- 38. de Gennes, P. G. & Prost, J. *The Physics of Liquid Crystals* (Clarendon, 1995).
- 39. Lavrentovich, O. D. Topological defects in dispersed words and worlds around liquid crystals, or liquid crystal drops. *Liq. Cryst.* **24**, 117–126 (1998).
- Volovik, G. E. & Lavrentovich, O. D. Topological dynamics of defects: boojums in nematic drops. *J. Exp. Theor. Phys.* 58, 1159–1167 (1983).
- 41. Lin, I.-H. et al. Endotoxin-induced structural transformations in liquid crystalline droplets. *Science* **332**, 1297–1300 (2011).
- 42. You, Z., Pearce, D. J. G., Sengupta, A. & Giomi, L. Mono- to multilayer transition in growing bacterial colonies. *Phys. Rev. Lett.* **123**, 178001 (2019).
- 43. You, Z., Pearce, D. J. G. & Giomi, L. Confinement-induced self-organization in growing bacterial colonies. *Sci. Adv.* **7**, eabc8685 (2021).
- Doi, M. & Edwards, S. F. Dynamics of rod-like macromolecules in concentrated solution. Part 2. J. Chem. Soc., Faraday Trans. 2 74, 918–932 (1978).
- 45. Basaran, M., Yaman, Y. I., Yüce, T. C., Vetter, R. & Kocabas, A. Large-scale orientational order in bacterial colonies during inward growth. *eLife* 11, e72187 (2022).
- Rumbaugh, K. P. & Sauer, K. Biofilm dispersion. *Nat. Rev. Microbiol.* 18, 571–586 (2020).
- Bottura, B., Rooney, L. M., Hoskisson, P. A. & McConnell, G. Intra-colony channel morphology in *Escherichia coli* biofilms is governed by nutrient availability and substrate stiffness. *Biofilm* 4, 100084 (2022).
- 48. Balaban, N. Q. et al. Definitions and guidelines for research on antibiotic persistence. *Nat. Rev. Microbiol.* **17**, 441–448 (2019).
- 49. Stewart, P. S. & Franklin, M. J. Physiological heterogeneity in biofilms. *Nat. Rev. Microbiol.* **6**, 199–210 (2008).

**Publisher's note** Springer Nature remains neutral with regard to jurisdictional claims in published maps and institutional affiliations.

Springer Nature or its licensor (e.g. a society or other partner) holds exclusive rights to this article under a publishing agreement with the author(s) or other rightsholder(s); author self-archiving of the accepted manuscript version of this article is solely governed by the terms of such publishing agreement and applicable law.

© The Author(s), under exclusive licence to Springer Nature Limited 2023

#### **Methods**

#### **Growth and imaging of confined biofilms**

The strains used in these experiments were derivatives of the C6706 El Tor strain and contained a point mutation in the diguanylate cyclase VpvC (vpvC<sup>W240R</sup>), which caused upregulated c-di-GMP production and therefore constitutive biofilm production<sup>25</sup>. Unless otherwise noted, these strains also included a deletion of the rbmA gene to isolate the effects of cell-cell adhesion<sup>50,51</sup>—this strain background was labelled WT\*. In addition to the WT\* strain, we also worked with a set of strains in which the genes encoding the adhesins Bap1 and RbmC were deleted. The  $\Delta bap1\Delta rbmC$  mutant exhibited little friction as it grew on the substrate<sup>16</sup>. We also used a set of strains that did not produce any extracellular polysaccharides through the deletion of the Vibrio polysaccharide synthase gene vpsL<sup>37</sup>, which behaved analogously to other non-biofilm-forming bacteria<sup>7,9-11</sup>. The bacteria were also genetically modified to constitutively express the fluorescent protein mNeon-Green or, in the case of cell trajectory measurements, mScarlet-I. For cell trajectory measurements, we used a strain containing mNeonGreen fused to the µNS protein from the avian reovirus, which self-assembled to form a single intracellular punctum. These puncta are inherited by one of the daughter cells while a new one self-assembles in its sibling, thereby allowing the tracking of cell trajectories over time<sup>36</sup>. For a complete list of strains, see Supplementary Table 1.

Biofilm growth experiments were performed in M9 minimal media (Sigma Aldrich) supplemented with 0.5% glucose (Sigma Aldrich), 2 mM MgSO<sub>4</sub> (JT Baker) and 100 μM CaCl<sub>2</sub> (JT Baker) (henceforth referred to as M9 media). For confined growth experiments, cells were first grown under shaken conditions overnight in LB broth (BD). The overnight culture was back-diluted 30× in M9 media and grown under shaken conditions until the optical density reached 0.05-0.25 (about 2 h). Concurrently, agarose polymer (Invitrogen) of a given concentration was boiled in M9 media and then placed in a water bath to cool to 40-50 °C without gelation. The bacterial culture was diluted in M9 media to an optical density of 0.001–0.003, and a 1 µl droplet of this diluted culture was deposited in the centre of a glass-bottomed 96-well plate (MatTek). The droplet was covered with 20 µl of the liquid agarose, which quickly solidified at room temperature and sandwiched the bacteria between the solidified gel and the glass substrate (note that we neglect the ~5% dilution of the agarose by the droplet). The gel mesh size was generally smaller than the cells, and therefore confined them, but large enough to allow free diffusion of nutrient and waste molecules. Finally, 200 ul of M9 media was added to the well on top of the solidified agarose to act as a nutrient reservoir. Cells were finally grown under static conditions at 30 °C and imaged at various times during development.

#### Overview of imaging and image analysis

Imaging was performed using a Yokogawa CSU-W1 spinning-disk confocal scanning unit mounted on a Nikon Ti2-E microscope body, using the Nikon perfect focus system, and images were acquired using Nikon Elements 5.20. For high-resolution, single-cell-level imaging, a 100× silicon oil immersion objective (Lambda S 100XC Sil, numerical aperture = 1.35) was used. At low agarose concentrations ( $c \le 0.5\%$ ), a z-step size of 0.195  $\mu$ m was used; at high agarose concentrations ( $c \le 0.5\%$ ), a z-step size of 0.13  $\mu$ m was used. For high-throughput biofilm morphology measurements, a 60× water immersion objective (CFI Plan Apo 60XC, numerical aperture = 1.20) and z-step size of 0.4  $\mu$ m were used. The green mNeonGreen fluorophore was excited using a 488 nm laser, the red mScarlet-I fluorophore was excited using a 640 nm laser and the far-red fluorescent beads were excited using a 640 nm laser. For time-course imaging, cells were incubated in a Tokai-Hit stage-top incubator at a temperature of 30 °C.

After acquisition, images were deconvolved using Huygens 20.04 (SVI). The high-resolution single-cell images were then segmented into individual cells using methods described elsewhere  $^{16,24}$ . Briefly, the images were first binarized layer by layer using an adaptive Otsu

method, and the cells were then segmented using an adaptive thresholding scheme (Extended Data Fig. 1). The cell locations and directions were then determined from the centre of mass and the principal axis from a principal component analysis of the segmented voxels, respectively. We further defined a cylindrical coordinate system where the origin was set by finding the radial centre of mass of all of the segmented cells.

#### High-throughput contact angle measurements

To attain high-throughput measurements of the contact angles across many biofilms, a large, tiled image, about 1 mm × 1 mm, containing  $27 \pm 20$  (mean  $\pm$  s.d., range 4–87) biofilms was first taken 2–6 hours after seeding to identify bacteria that started at the gel-substrate interface and then taken 12–20 hours after seeding for contact angle ( $\psi$ ) measurement. Since we were only interested in measuring the effective  $\psi$ , we restricted our attention to the bottom 5 µm of each biofilm in this assay. The images were deconvolved and then segmented using a custom Matlab (v.2018a) script. First the images were denoised and binarized layer by layer using a Wiener two-dimensional adaptive noise-removal filter and Otsu thresholding. Biofilms were then either automatically or manually identified as large, connected binarized voxels. For each biofilm and for each layer, a convex hull that contained all binarized pixels was found, and the area of the hull was taken to be the cross-sectional area of the biofilm A(z) at each height z. From the cross-sectional area, the effective radius was calculated as  $r(z) = (A(z)/\pi)^{1/2}$ . The contact angle was then found by fitting a linear slope and calculating  $\psi = \tan^{-1}(dr/dr)$ dz) + 90° (Extended Data Fig. 2).

#### Tracing of cell trajectories

To trace the cell trajectories in the biofilm, we tracked the trajectories of individual puncta inside the biofilm. First, the deconvolved images were registered using Matlab built-in functions to minimize frame-to-frame jitter. Individual puncta were then identified as local maxima in the images, and subpixel resolution was attained by fitting a parabola around each maximum. This process was repeated for all frames, and the particles were connected over time using TrackMate particle-tracking software <sup>52</sup>. These puncta trajectories were projected into the cylindrical coordinates of the biofilm. The averaged trajectories were calculated by averaging all trajectories whose final coordinate (r,z) was within 3  $\mu$ m of the target final coordinate (r,z) was within 3  $\mu$ m of the target final coordinate trajectories were averaged. The final target coordinates were chosen at different points near the boundary.

#### Visualization of the gel deformation

To visualize the deformation of the agarose gel, we diluted 200 nm far-red fluorescent particles (Invitrogen) at a ratio of 1:100 into the molten agarose gel before encasing the bacteria. In the first step of the data analysis process, a portion of the deconvolved images where little particle motion was expected was used to register the images using Matlab built-in functions. Using a procedure similar to puncta tracking, the fluorescent particles were identified and tracked by finding local maxima and using the TrackMate particle-tracking software. The 'age of the interface' was determined by finding the time when the vertical displacement of particles near the substrate (initially within 5  $\mu$ m) exceeded a threshold value of 0.5  $\mu$ m, corresponding to a local delamination event.

#### Quantification of cell ordering

To quantify the average cell ordering inside the biofilms, we averaged cell directions using the Q-tensor model of LCs $^{53}$ . For each cell i, we first converted the direction into a head-tail symmetric quantity by taking the outer product of the direction with itself,  $Q_i = (3\hat{\mathbf{n}}_i \otimes \hat{\mathbf{n}}_i - I)/2$  (where  $\hat{\mathbf{n}}_i$  is in cartesian coordinates). Each biofilm was discretized into cylindrical sectors with  $\Delta r = 2 \, \mu \mathrm{m}$ ,  $\Delta z = 2 \, \mu \mathrm{m}$  and  $\Delta \theta = \pi/4$ , and Q was

then averaged in each sector, yielding a locally averaged, spatially varying nematic order parameter  $Q(r,\theta,z)$ . To azimuthally average Q, we first converted the tensor to cylindrical coordinates through the transformation  $Q_p = R^T Q R$ , where R is the transformation matrix and  $R^T$  its transpose, and then averaged across  $\theta$ . Finally, to average across many biofilms at the same agarose concentration, we rescaled each biofilm by its maximum radius and height, yielding  $Q_p\left(\frac{r}{r_{mv}},\frac{z}{z_{mv}}\right)$ , and

then averaged  $Q_{\rm p}$  across many biofilms. To visualize and quantify the nematic order parameter, we calculated the scalar order parameter S as the maximum eigenvalue of Q,  $Q_{\rm p}$  or  $\bar{Q}_{\rm p}$  and  $\hat{\bf n}$  as the corresponding eigenvector.

#### **Agent-based simulations**

The ABSs were built on those developed in <sup>16</sup> and updated to include cell–gel adhesion. For details, see Supplementary Note 1.

#### Continuum modelling of biofilm shape morphogenesis

A continuum model for the macroscopic morphogenesis of *V. cholerae* biofilms confined between an infinite elastic material and a hard substrate was developed. For details, see Supplementary Note 2.

#### **Data availability**

All relevant data supporting the key findings of this study are available in the article and its Supplementary Information files or from the corresponding authors upon reasonable request. Raw image data can be accessed via https://doi.org/10.5061/dryad.9kd51c5nw. Source data are provided with this paper.

#### **Code availability**

The ABSs were implemented in the framework of the molecular dynamics simulator LAMMPS and can be retrieved from https://zenodo.org/record/7879038#.ZE0-US\_MKJ8. Images were analysed using custom-written Matlab codes (v.2018a) and can be retrieved from https://doi.org/10.5281/zenodo.5570867.

#### References

- Fong, J. C. N., Karplus, K., Schoolnik, G. K. & Yildiz, F. H. Identification and characterization of RbmA, a novel protein required for the development of rugose colony morphology and biofilm structure in Vibrio cholerae. J. Bacteriol. 188, 1049–1059 (2006).
- 51. Fong, J. C. et al. Structural dynamics of RbmA governs plasticity of *Vibrio cholerae* biofilms. *eLife* **6**, e1002210 (2017).
- Tinevez, J.-Y. et al. TrackMate: An open and extensible platform for single-particle tracking. Methods 115, 80–90 (2017).

53. Cates, M. E. & Tjhung, E. Theories of binary fluid mixtures: from phase-separation kinetics to active emulsions. *J. Fluid Mech.* **836**, P1 (2018).

#### **Acknowledgements**

We thank R. Alert, R. Long, R. Zhang and N. Goldenfeld for helpful discussions. Research reported in this publication was supported by the National Institute of General Medical Sciences of the National Institutes of Health under Award Number DP2GM146253 (J.Y.). J.Y. holds a Career Award at the Scientific Interface from the Burroughs Wellcome Fund (1015763.02). This publication was made possible in part with the support of the Charles H. Revson Foundation 22-28 (J.N.). J.-S.B.T. is a Damon Runyon Fellow supported by the Damon Runyon Cancer Research Foundation (grant no. DRG-2446-21). T.C. acknowledges the support of T. B. Bentley, Office of Naval Research Program Manager, under award number N00014-20-1-2561. S. Zhou acknowledges the support of NSF CAREER award, DMR-2239551.

#### **Author contributions**

J.N. and C.L. contributed equally to the work. J.N. and J.Y. conceptualized the project. J.N. and Q.Z. performed the experiments, and J.N. and J.-S.B.T. performed the data analysis. J.N., M.K., T.H., S. Zhou, T.C. and J.Y. formulated the theoretical model. C.L. and S. Zhang developed the ABSs. All authors contributed to the writing of the paper. Correspondence and requests for materials should be addressed to J.Y., T.C. or S. Zhang.

#### **Competing interests**

The authors declare no competing interests.

#### **Additional information**

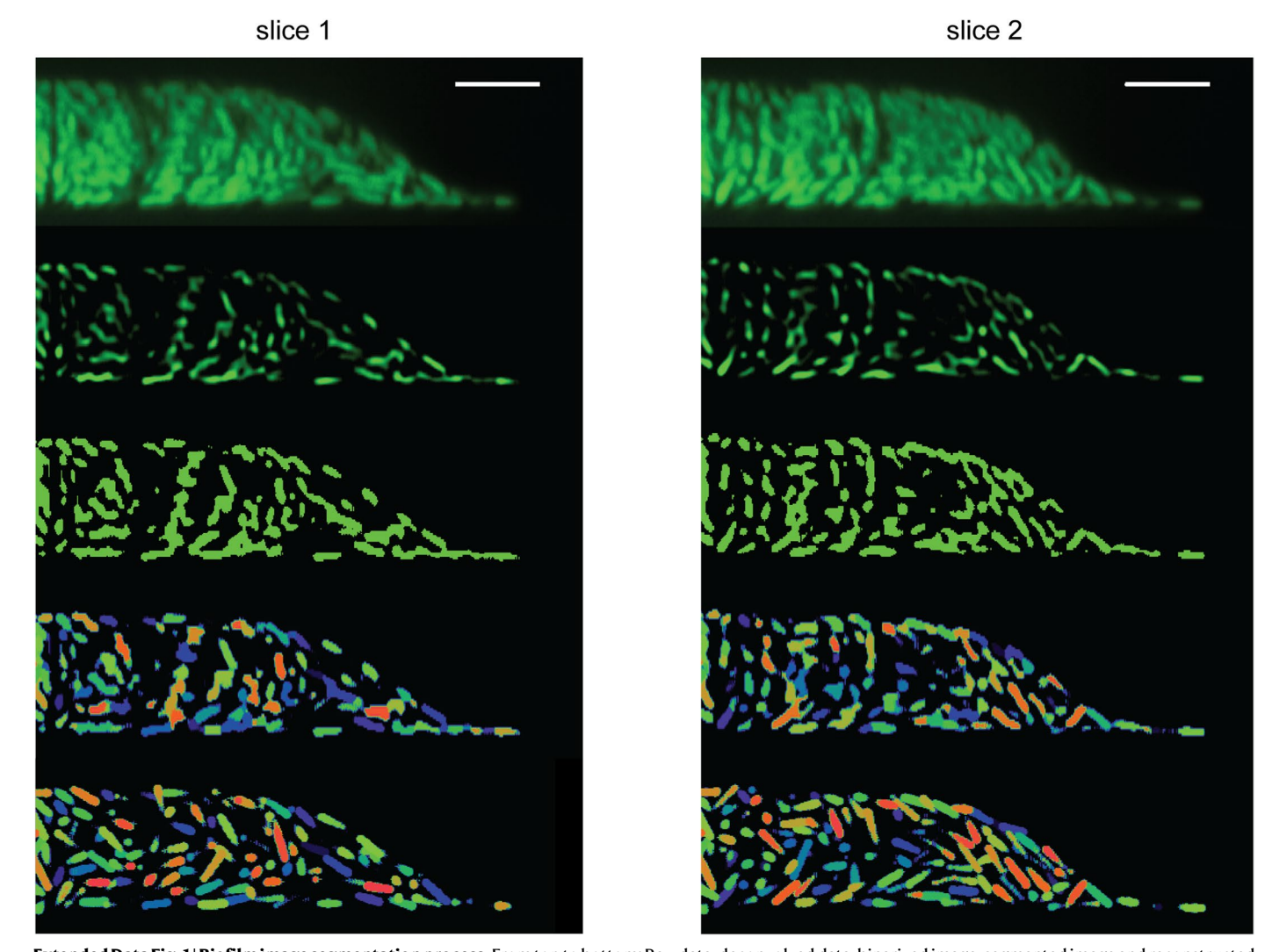
**Extended data** is available for this paper at https://doi.org/10.1038/s41567-023-02221-1.

**Supplementary information** The online version contains supplementary material available at https://doi.org/10.1038/s41567-023-02221-1.

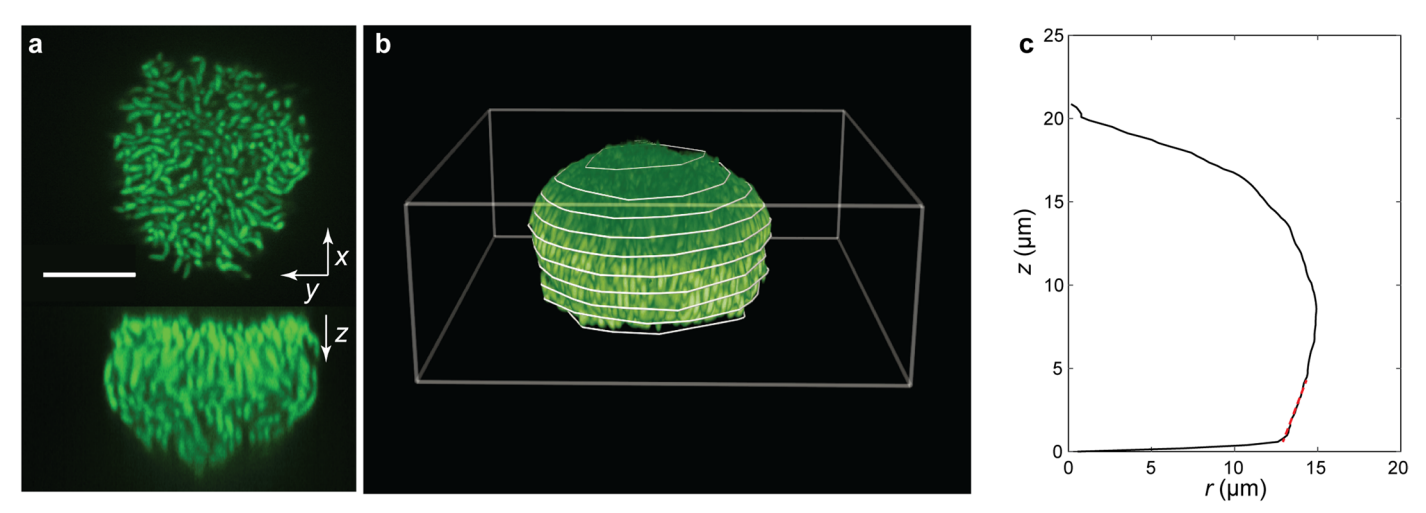
**Correspondence and requests for materials** should be addressed to Tal Cohen, Sulin Zhang or Jing Yan.

**Peer review information** *Nature Physics* thanks Vernita Gordon and the other, anonymous, reviewer(s) for their contribution to the peer review of this work.

**Reprints and permissions information** is available at www.nature.com/reprints.

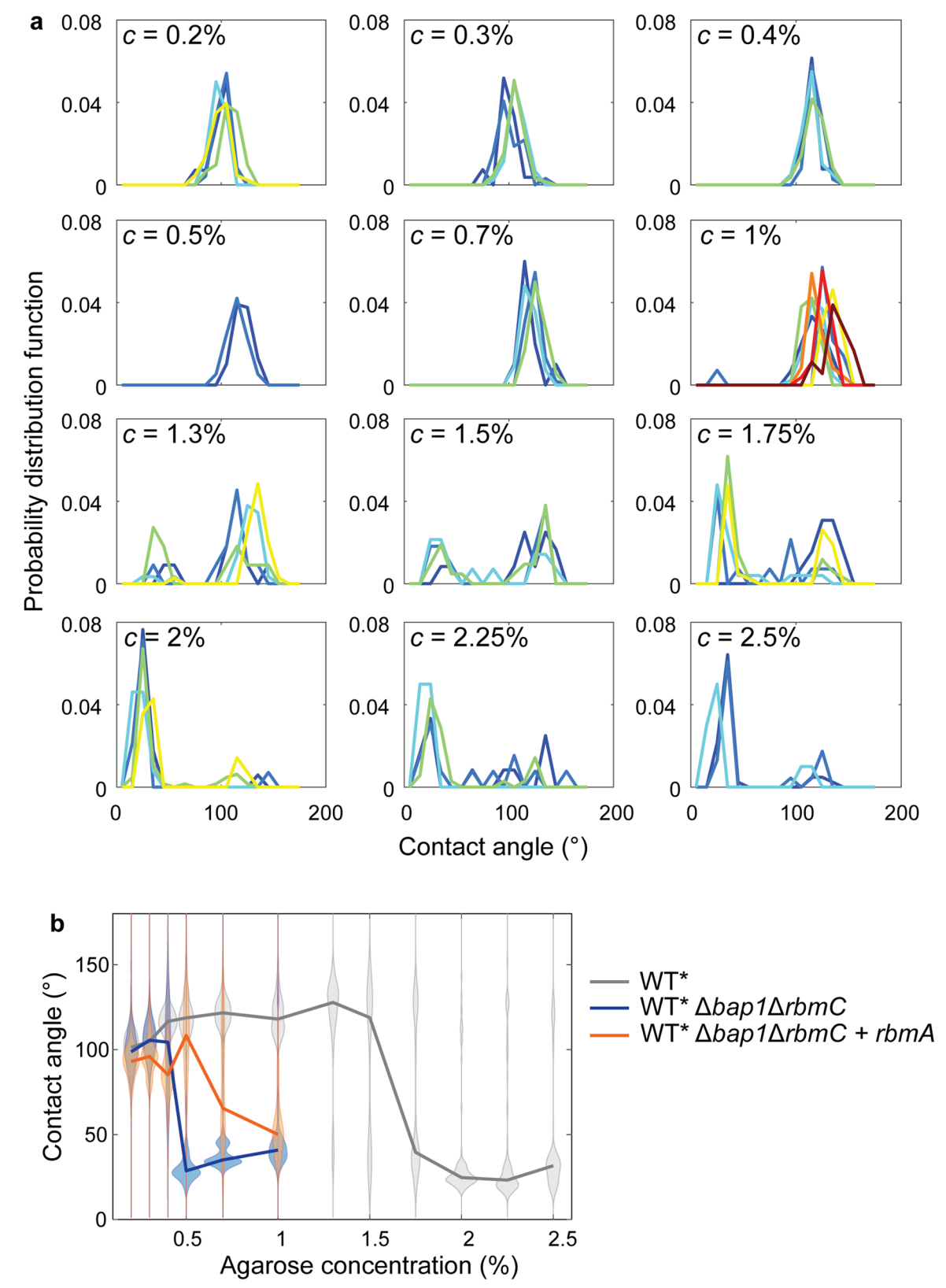


**Extended Data Fig. 1**| **Biofilm image segmentation process.** From top to bottom: Raw data, deconvolved data, binarized image, segmented image and reconstructed image. In the bottom two panels, each colour denotes a distinct cell. Slice 1 and slice 2 correspond to two different (r, z) cuts of the same biofilm grown under a 2% gel overnight. Scale bar, 5  $\mu$ m.



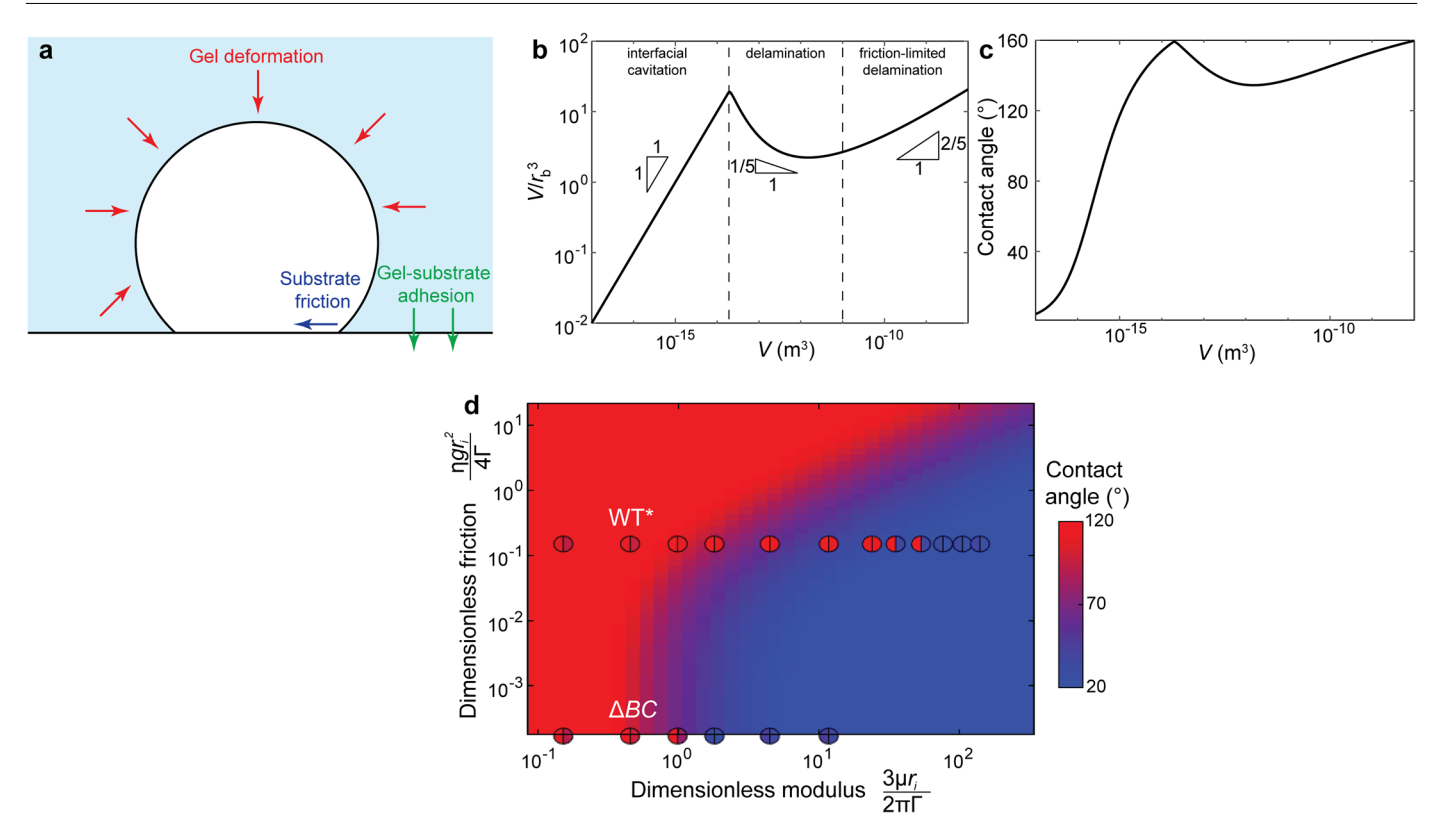
**Extended Data Fig. 2** | **Example biofilm and contour identification.** (a) Raw image showing the basal plane (top) and cross-section (bottom) of a WT\* biofilm grown under a 0.5% agarose gel. Scale bar, 10  $\mu$ m. (b) Three-dimensional reconstruction of the biofilm in (a) with the areal convex hulls

overlain (white). (c) Effective radii of the convex hulls as a function of the height of the biofilm. Red line corresponds to a linear fit from which the effective contact angle is calculated.



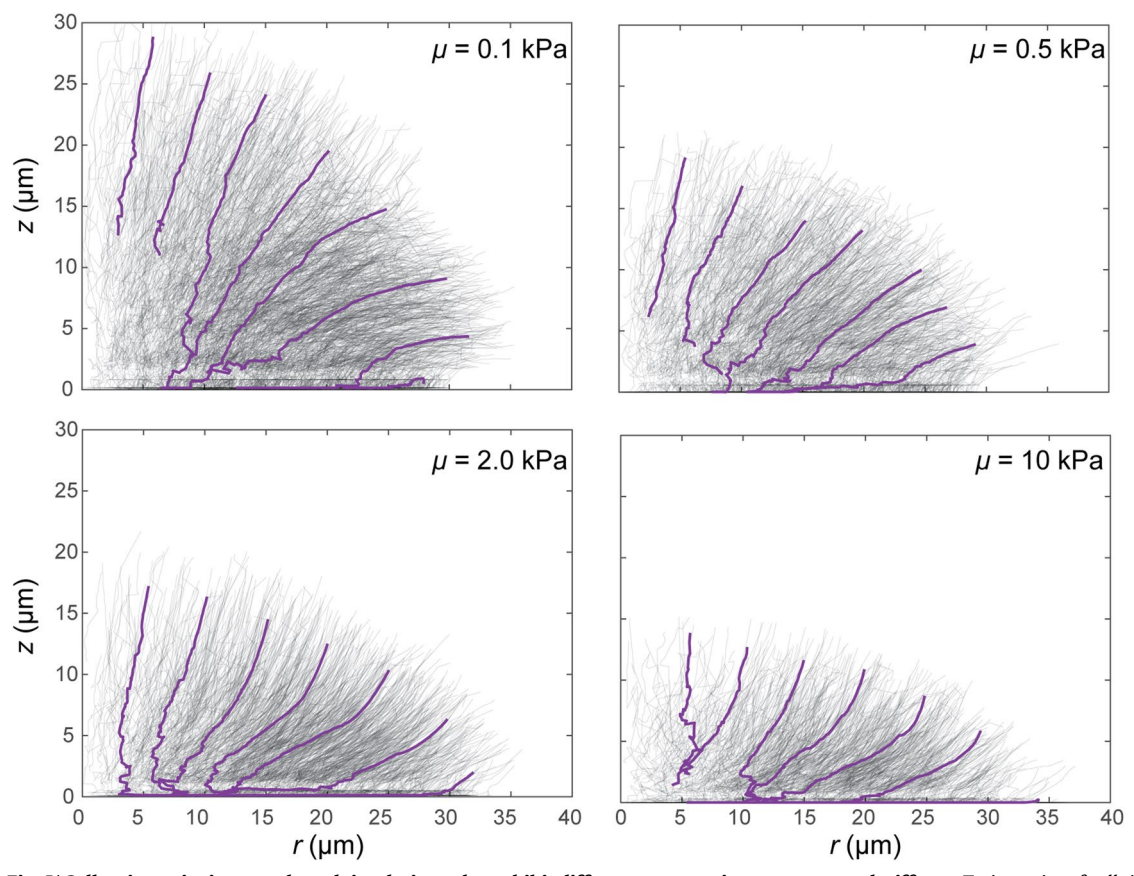
**Extended Data Fig. 3 | Contact angle distributions across experiments and mutant strains. (a)** Probability distribution function of different contact angles for biofilms grown under gels of different agarose concentrations. Each line corresponds to a distinct single field of view with at least 10 biofilms. In general, we find that the distributions, including the bimodal distributions at intermediate concentrations, are well preserved across experiments. (b) Violin plot of contact angles calculated for biofilms formed by different mutant strains

grown under gels of different agarose concentrations. Each chord represents a probability distribution and the lines connect the median values of the distributions. The grey data correspond to the data in Fig. 1c, the blue data are for a mutant strain that lacks biofilm adhesins Bap1 and RbmC and the orange data are for a mutant strain that also lacks biofilm adhesins Bap1 and RbmC but expresses the cell-cell adhesin RbmA. We note that the cell-cell adhesion seems to minimally affect the shape transition.



**Extended Data Fig. 4** | **Competition between gel stiffness and substrate friction controls biofilm morphogenesis.** (a) Schematic of the theoretical setup. A biofilm with basal radius  $r_b$  sits at the interface of a rigid bottom substrate and a semi-infinite elastic gel (blue). As the biofilm grows, its expansion is impeded by friction from the substrate; meanwhile, the growth of the biofilm deforms the gel around it, potentially delaminating the gel from the substrate. (b, c) Example solutions showing the evolution of the rescaled volume  $V/r_b^3$  (b) and contact angle (c) for  $\mu = 3$ kPa and  $\eta = 10^{11}$ Pa s/m. Experimentally, the initial

regimes are difficult to observe because of errors in defining the shape of a biofilm consisting of tens of cells. (**d**) Predicted biofilm contact angle as a function of dimensionless substrate friction and gel modulus. Overlain circles denote the experimental results from Extended Data Fig. 3. The two halves of each circle quantify the interquartile range of measured contact angles. The adhesin-less mutant  $\Delta bap1\Delta rbmC$  ( $\Delta BC$ ) has a negligible dimensionless friction value and is therefore plotted on the x-axis.



Extended Data Fig. 5 | Cell trajectories in agent-based simulations also exhibit different patterns in response to gel stiffness. Trajectories of cells in agent-based simulations with different gel stiffnesses show two different types of patterns: either curving down leading to fountain-like trajectories (top) or curving up (bottom), consistent with experimental observations.

60

60

60

 $\Delta z$ 

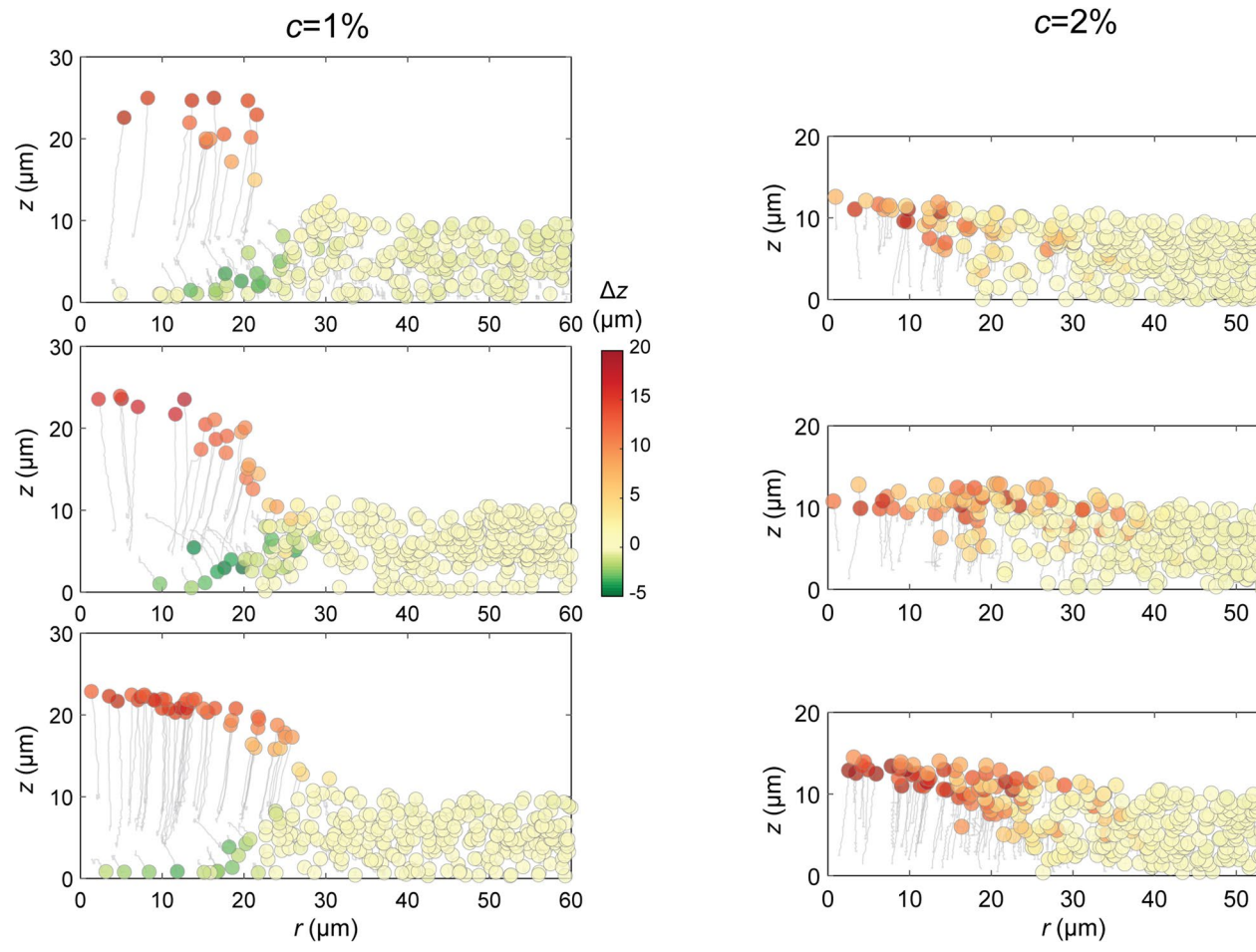
(µm)

10

5

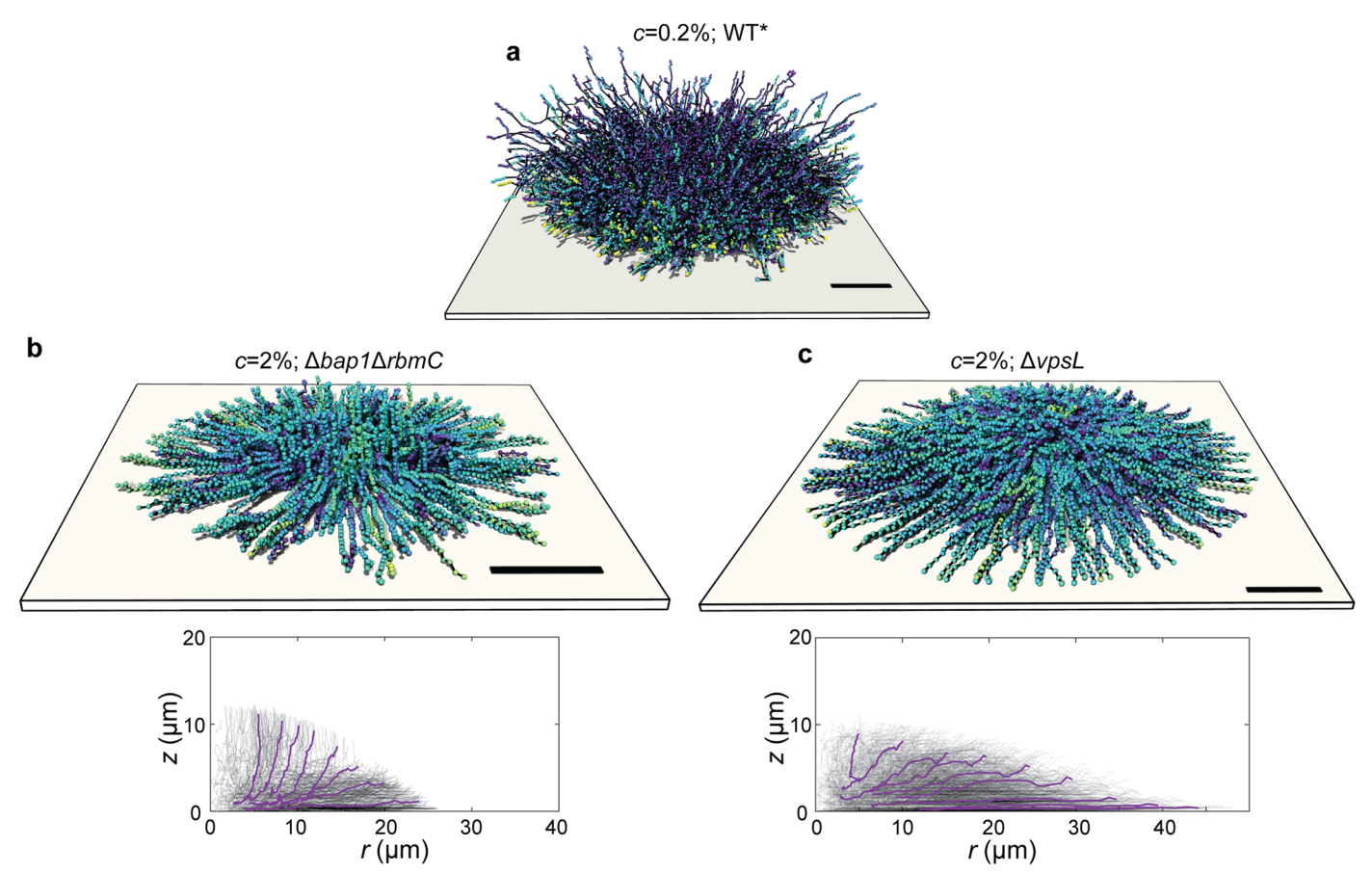
0

-5



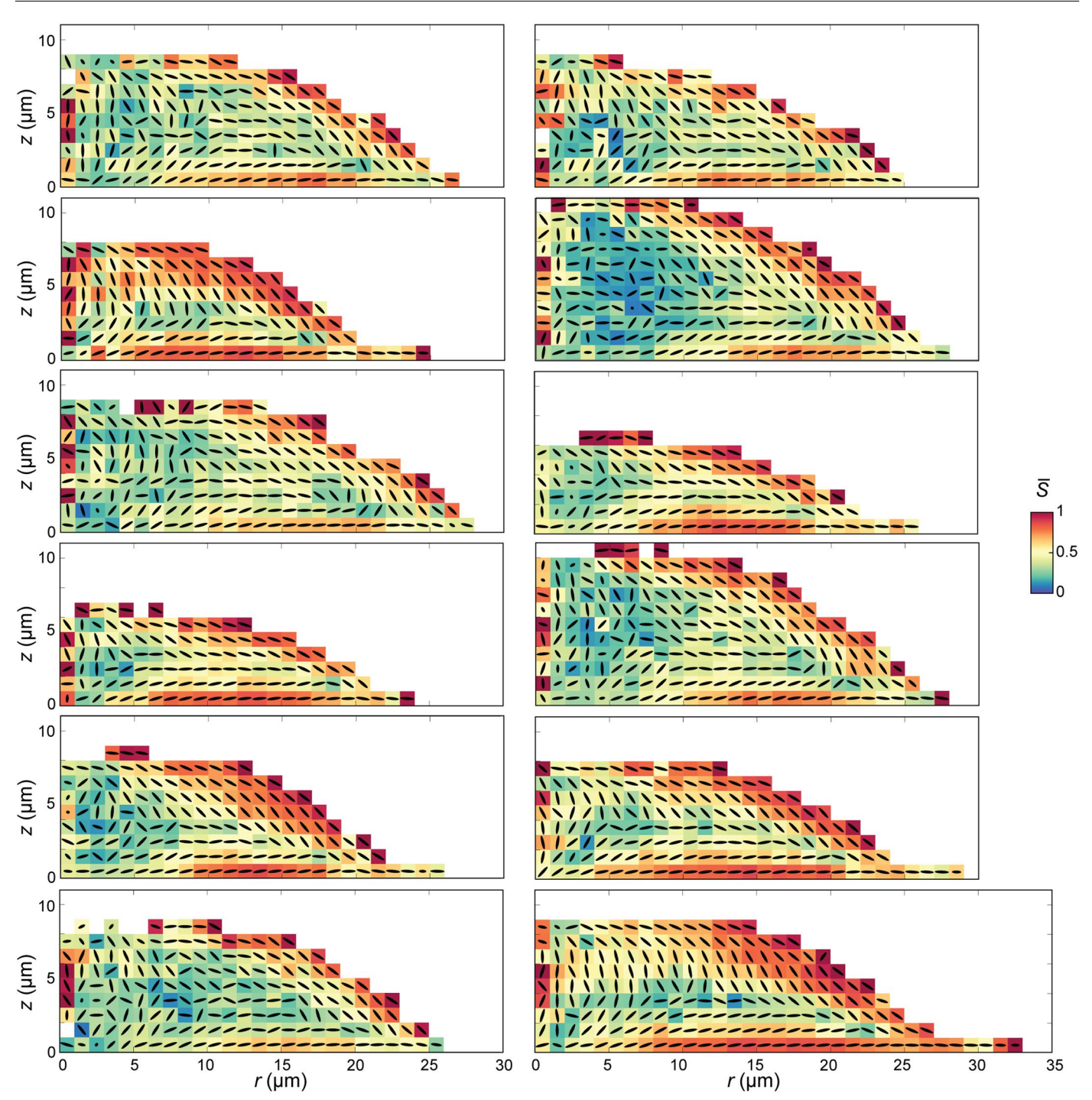
**Extended Data Fig. 6 | Distinct gel deformation modes for dome- and lens-shaped phenotypes.** Displacement of tracer particles in the axisymmetric coordinates of the biofilm during growth of 6 different biofilms. The colours denote the direction and magnitude of the vertical displacement of the beads at

the end of the experiment with respect to their original locations (z(t)-z(0)). Consistent with the interfacial cavitation model for the growth of dome-shaped biofilms, we observed negative values near the boundary, corresponding to gel materials that are compressed and therefore move closer to the glass substrate.



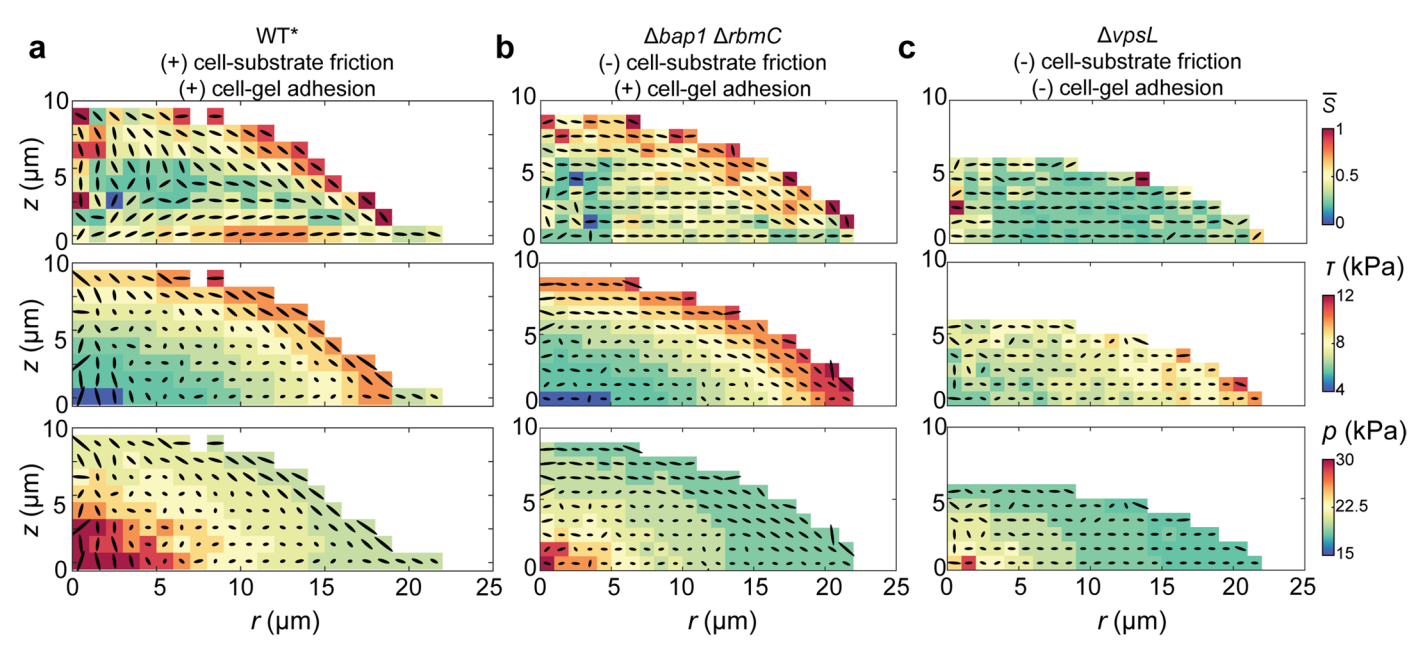
**Extended Data Fig. 7** | **Cell trajectories in mutant biofilms. (a)** Reconstructed puncta trajectories for a WT\* biofilm grown under a soft gel (corresponding to averaged data in Fig. 3b). Scale bar,  $10~\mu m$ . (b, c) 3D reconstructed puncta trajectories (top) and projected and averaged trajectories (bottom) for a biofilm that does not produce the extracellular adhesins Bap1 and RbmC (b) and for bacteria that do not produce any extracellular matrix ( $\Delta vpsL$ , c) grown under a stiff gel (c=2%). While the  $\Delta bap1\Delta rbmC$  mutant (b) follows similar trajectories as the WT\* biofilm under a stiff environment (Fig. 3b), trajectories of  $\Delta vpsL$  cells

exhibit the opposite curvature. It has been shown previously that the  $\Delta bap1\Delta rbmC$  mutant still retains some adhesion to the top gel surface through the exopolysaccharide, which is critical to create the upward bending of the cell trajectories. In contrast, the  $\Delta vpsL$  mutant exhibits a trajectory that can be expected if all regions of the biofilm are growing in dimensions proportional to the growing radius and height. These results support the conclusion that biofilm shape and biofilm-gel adhesion jointly dictate the cell trajectories in a biofilm.



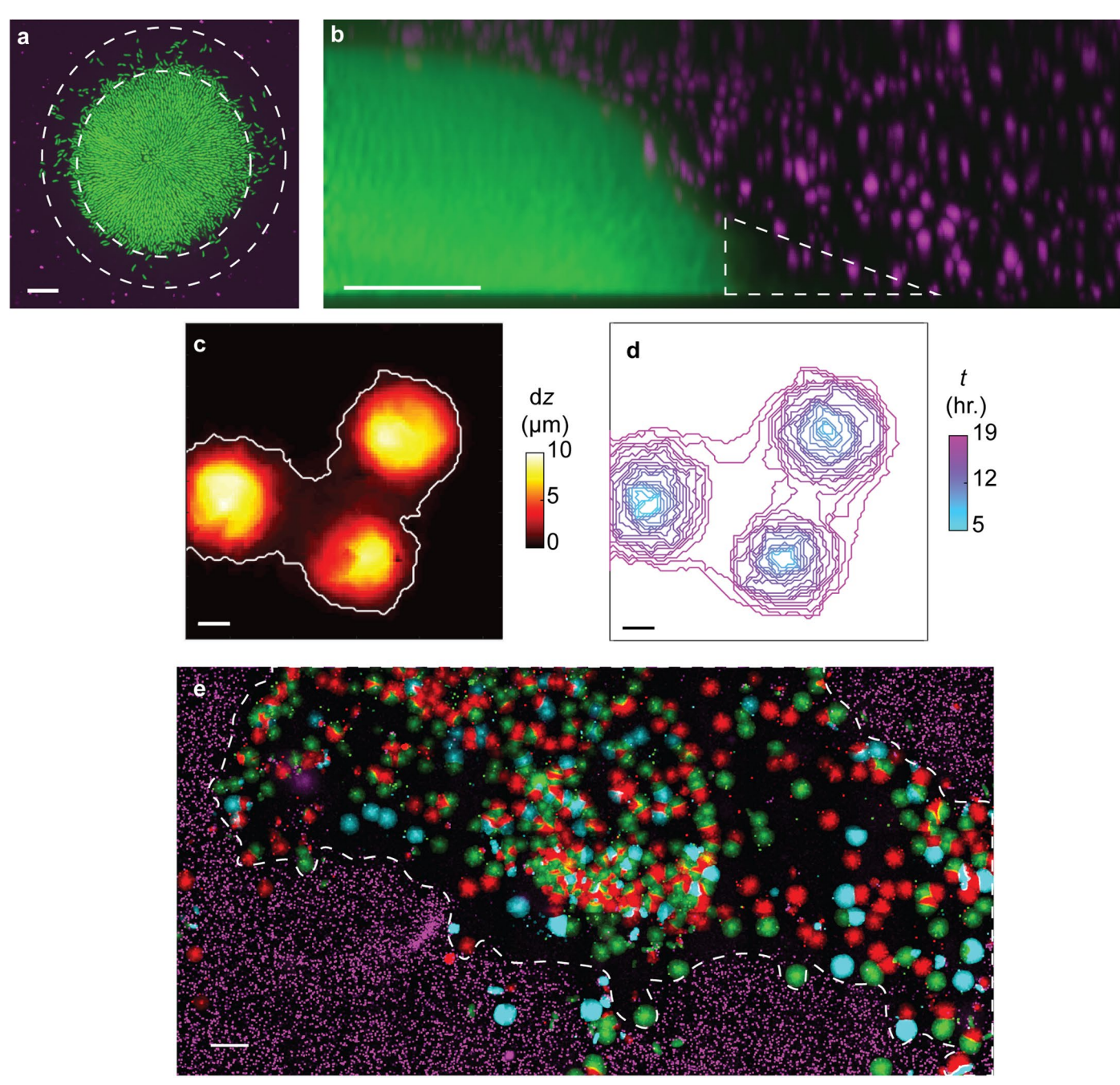
Extended Data Fig. 8 | Bacteria reproducibly self-organize into the same overall biofilm architecture. Azimuthally averaged cell orientations for WT\* biofilms grown under 2% gels overnight. Colours denote the nematic order parameter and the ovals denote the average director of the cells projected into

(r,z) space. Each panel corresponds to a unique biofilm of different size but yields the same overall cellular ordering. These data were rescaled and averaged to give the prototypical organization shown in Fig. 5b in the main text.



Extended Data Fig. 9 | Agent-based simulations for WT\* and mutant biofilms grown under a gel with  $E=3\times10^4$  Pa. Top: azimuthally averaged cell orientations (black oval) and nematic order parameter (color). Middle: first principal stress direction (black oval) and shear stress distribution (color). Bottom: first principal stress direction (black oval) and pressure distribution (color). Results are shown

for (a) a biofilm with cell-substrate friction and cell-gel adhesion, corresponding to WT\* biofilms in the experiments; (b) a biofilm with cell-gel adhesion only, corresponding to  $\Delta bap1\Delta rbmC$  mutant biofilms in the experiments; (c) a colony with neither cell-substrate friction nor cell-gel adhesion, corresponding to  $\Delta vpsL$  mutant colonies in the experiments.



**Extended Data Fig. 10** | **Collective delamination enables dispersed cells to explore new territories.** (a) Basal layer of a biofilm, with dispersed cells around it (enclosed by the dashed lines). (b) Radially averaged intensity plot corresponding to the biofilm in (a). The green intensity corresponds to the azimuthally averaged signal from the fluorescently labelled bacteria, and the magenta corresponds to the azimuthal maximum intensity projection of the tracer particles. Empty space is observed between the glass and gel beyond the edge of the biofilm, highlighted by the dashed triangle. (c) Displacement *dz* of the agarose gel nearest to the substrate relative to its initial position. The three peaks correspond to three biofilms which have collectively delaminated the gel

from the substrate. The white outline corresponds to the 0.5  $\mu m$  contour of dz. (d) Evolution of the delaminated region (the 0.5  $\mu m$  dz contour) over time, showing initially local growth before collective delamination. (e) Image of the basal layer of many biofilms, showing collective delamination. The initial inoculation consisted of three differently coloured but otherwise identical WT\* strains. The magenta dots correspond to tracer particles embedded in the gel near the basal plane, the absence of which coincides with the absence of agarose gel – this collectively delaminated region is outlined by the dashed line. Scale bar in a,b,c,d, 10  $\mu m$ ; scale bar in e, 100  $\mu m$ .